

This is a preprint of the following article, which is available at: <http://mdolab.engin.umich.edu>
G.W. Ng, J. R. R. A. Martins, and Y. L. Young. Optimizing steady and dynamic hydroelastic performance of composite foils with low-order models. *Composite Structures*, 301(6):116101, December 2022.

The original article may differ from this preprint and is available at:
<http://dx.doi.org/10.1016/j.compstruct.2022.116101>.

Optimizing steady and dynamic hydroelastic performance of composite foils with low-order models

Galen W. Ng, Joaquim R. R. A. Martins, and Yin L. Young

*Department of Naval Architecture & Marine Engineering, University of Michigan,
Ann Arbor, MI, 48109*

Department of Aerospace Engineering, University of Michigan, Ann Arbor, MI, 48109

*Department of Mechanical Engineering, University of Michigan, Ann Arbor, MI,
48109*

Abstract

Predicting and controlling the steady and dynamic hydroelastic performance is a crucial challenge in marine composite lifting surface design. Excessive flow-induced vibrations and accelerated fatigue can be severe issues if not considered in the initial design. Most design optimizations only consider steady performance and neglect critical dynamic aspects of the marine environment, such as lower resonance frequencies and different band gaps between modal frequencies in water compared to in air. This work uses lower-order models to capture the steady and dynamic fluid-structure interaction behavior and optimize the design of composite hydrofoils. We formulate new objectives and constraints that consider the natural frequencies, damping, and frequency response spectra in addition to steady hydroelasticity to achieve the design intent. The optimization method is heuristic, which is appropriate for this level of model fidelity where holistic parameter trends are more of interest. Results for a 1/3 length-scale hydrofoil model showed a significant improvement in the optimized performance over the baseline. By tailoring geometric and material variables of the composite hydrofoil, we produced an optimal design. This design meets the steady design condition requirements and avoids excessive vibrations and dynamic load amplifications due to lock-in, resonance, flutter, and modal coalescence.

1 Introduction

Lifting surfaces are widely used in the maritime sector in energy harvesters, energy saving devices, rudders, propellers, bilge keels, fin stabilizers, hydrofoils, and more. They are critical components that impact the overall performance and efficiency of marine vessels and platforms. Compared to traditional metallic marine structures, composites offer many benefits to lifting surface design, such as lower structural weight, reduced manufacturing cost, and material anisotropy [1, 2]. Through careful design of the fiber layups, one can tailor the load-dependent static hydroelastic response at multiple operating conditions to improve the overall efficiency compared to rigid lifting surfaces [3]. Interest in marine composite lifting surfaces has increased because of advances in computational modeling, manufacturing techniques, and materials science.

The dynamic fluid-structure interaction (FSI) response of aircraft wings has been researched thoroughly in the last several decades [4]. However, the dynamic FSI response of marine composites is still not well understood. Because the fluid density of seawater is about 850 times that of air, the hydrodynamic loading is significant for a given flow speed compared to aerodynamic loading. Marine lifting surfaces are typically solid construction and have much smaller aspect ratios (AR) than aircraft lifting surfaces to withstand such loads, which can also lead to complicated 3D geometries and junctions. Marine composites must be designed to withstand steady and dynamic loads. Examples of external unsteady excitations include waves, vortex shedding, cavitation, ventilation, and vessel motions. Cavitation erosion is particularly damaging to composites [5]. Furthermore, high-speed vessels are subject to extreme conditions because fluid loading increases with speed squared. Surface vessels are particularly susceptible to extreme vessel motions coupled with cavitation and ventilation on the lifting surfaces [6]. The International Towing Tank Conference (ITTC) 2021 Seakeeping Committee [7] noted increased research into the design of high-speed craft, particularly foiling and foil-assisted craft, potentially due to the recent popularity of high-profile sailing competitions featuring foiling craft. Therefore, understanding, predicting, and then optimizing the hydroelastic performance of composites is essential to the safety and efficiency of the next generation of high-speed surface craft.

The dynamics of marine structures differ from aircraft structures because of the high density of water that leads to much lower resonance frequencies because of fluid-added mass effects [1, 8]. Multiphase flows, such as cavitation and ventilation, also complicate fluid-added mass effects because the surrounding fluid is mostly a mixture of water and vapor for cavitation, and water and noncondensable gas in the case of ventilation [6, 8, 9]. The multiphase flow regime affects the spatial and temporal distribution of the gaseous cavity on the lifting surface and thus the added mass effects. Fluid-added mass depends on the direction of motion, resulting in different band gaps between modal frequencies than those in air. Fluid-added mass in water can result in modal coalescence or mode reordering due to changes in submergence, speed, or flow regime [8, 10–13].

General dynamic phenomena categories for marine lifting surfaces include lock-in, resonance, modal coalescence, and flutter. These are undesired because they can lead to excessive vibrations and dynamic load amplification, which affect passenger discomfort,

control of the lifting surface and vessel, and fatigue. The fatigue performance of marine composites is particularly challenging to predict compared to metallic marine structures because of uncertainty due to the environmental and manufacturing factors [14]. *Lock-in* can occur when an external oscillation frequency is close to one of the system natural frequencies and locks into it; examples include lock-in due to waves, vortex shedding [15], and cavity shedding [16]. *Classical resonance* is an externally excited instability similar to lock-in, but the external frequency matches the system natural frequency. In *parametric resonance*, system parameters modulate at half multiples of one of the system natural frequencies leading to exponential growth in deformations and dynamic load amplifications much higher than classical resonance [17]; a marine example is system mass modulation on hydrofoils due to unsteady multiphase flows [8, 18]. *Coalescence* occurs when two system natural frequencies converge on each other resulting in dynamic load amplifications. Changes in submergence due to body motions, wave oscillations, and flow regime changes can all affect modal coalescence. The coalescence of adjacent modes can manifest as severe dynamic load amplifications much higher than from the excitation of the separated modes [15]. *Flutter*, on the other hand, is a self-excited dynamic instability generally defined as when the damping of a system mode becomes zero or negative, leading to oscillations that grow with time.

Marine composites have different FSI owing to the low ratio of structural density to fluid density (μ). For low μ , a new, low-frequency dynamic instability mechanism arises at sufficiently high flow speeds because the disturbing fluid force increases with speed squared, while solid elastic restoring forces remain constant. relative magnitudes between the fluid and structural forces. This was first observed in hydrofoil experiments by Besch and Liu [19], and they called it the ‘new mode’. Akcabay and Young [20] were the first to predict it in simulation and its origin in water, which is from coupled, speed-dependent, quasi-steady (i.e., damping and stiffness) hydrodynamic memory terms in the equations of motion. At sufficiently high speeds, the low-frequency pole (a.k.a. mode) emerges that can potentially undergo a primarily bending-mode flutter as speed increases to the critical speed. The instability of the low-frequency ‘new mode’ is dangerous by itself, but it is also dangerous for marine craft because vessel rigid-body natural frequencies and wave excitation frequencies tend to be low as well; the elastic and rigid-body modes can potentially interact and accelerate an instability called *body-freedom flutter (BFF)*.

Most prior research has optimized the steady FSI of marine composite lifting surfaces [3, 21–25] in fairly high-fidelity; it is important to consider steady hydrodynamic efficiency (i.e., lift-to-drag ratio), static deflections, composite material failure modes, cavitation inception, ventilation inception, flow separation, and effects of free-surface and depth on the performance. Hydrodynamic efficiency is essential across the speed envelope, but any constraints on the steady failure modes or flow regime transition typically occur at high-angle, high-speed conditions. Designing a composite hydrofoil to optimize the steady performance subject to the steady constraints is an essential starting point. However, the dynamics must be considered for a complete hydroelastic design optimization. Dynamic FSI, on the other hand, considers the fluctuating performance, which is more easily explained through generalized fluid forces (i.e., fluid-added mass, hydrodynamic damping, fluid de-stiffening forces), and how that is intertwined

with the structural dynamics; dynamic FSI is important to vibrations, noise, dynamic load amplifications, accelerated fatigue, and dynamic instabilities—examples of which were given previously.

The goal now is to control the dynamic hydroelastic performance of a composite hydrofoil in addition to the steady performance since few works have addressed the dynamic optimization for composite hydrofoils. Some prior related research is as follows. Structural engineers have optimized topology to minimize vibrations due to external excitations [26]. The review by Niu et al. [26] discussed objective functions, such as weighted average surface displacements, dissipated power, local structural response, and acceleration of the structure. He et al. [27] minimized hub vibrations of marine composite propellers, where they used a non-dimensionalized sum of the force and moment amplitudes at the hub as the objective function. They considered the spatially varying wake behind a hull. However, they only optimized the layup and fiber direction at a fixed advance coefficient, so they neglected shape variables and the effects of changing propeller blade rate frequencies. Mulcahy et al. [28] performed hydroacoustic design optimization using emitted sound power as the objective to minimize for composite propellers at a fixed rotation rate and only using the layup and fiber angles as design variables. Many formulations relied on the excitation spectra and operating conditions staying constant, which we know for a hydrofoil on a vessel is not since the vessel is never sailing in steady, fixed conditions. Bachynski et al. [29] considered the time-varying aspect and optimized the annual power takeoff of a wave-energy converter by tuning resonance characteristics. However, their work depended on frequency response spectra, and a designer may sometimes know only the critical frequencies to avoid. Lastly, Jonsson et al. [30] formulated smooth flutter constraints for aircraft based on system eigenvalues and aggregation methods. As far as the authors know, hydrostructural optimization considering frequency coalescence has not been addressed in any work. This might be because the frequency coalescence of marine composites in high-speed surface craft has only recently been recognized as a critical instability [8, 12, 15].

This work aims to optimize the steady and dynamic performance of composite hydrofoils using lower-order models. Lower-order models are cheap to evaluate and give holistic insights into design trade studies, so they are appropriate for this preliminary work on understanding how to tailor the steady and dynamic performance of hydrofoils. We devise multipoint objective functions and steady and dynamic constraints to capture the speed-dependent effects on the system’s dynamic response and avoid excessive flow- and system-induced vibrations caused by cavity shedding frequencies, propulsor blade and shaft rates, engine frequency, and rigid body resonance frequencies.

2 Problem formulation

2.1 Computational model

Dynamic Composite Foil (DCFoil) is a lower-order, composite hydrofoil model first developed by Akcabay and Young [20]. It has been experimentally validated against published aeroelastic and hydroelastic results [20, 31, 32]. DCFoil was also able to

predict the emergence of the low-frequency ‘new mode’ first observed in hydrofoil experiments [20, 32] that originates from shed vortices with hydrodynamic memory effects (see Section 1). Modifications to this model include the usage of semi-empirical equations for the cavity-induced loading on flexible composite foils, which were validated by Young et al. [33]. We model the hydrofoil as a canonical cantilevered beam, which can represent a variety of structures such as rudders, fins, portions of a T-foil, and propeller or turbine blades. We use potential flow theory and Euler-Bernoulli beam theory for the structure with consideration for structural warping. We use frequency-domain, unsteady hydrodynamic strip theory with modifications for 3D flow effects to account for sweep (Λ) and finite span (s).

Each spanwise section has two degrees of freedom (DOF), bending (w) and twisting (ψ), defined about the elastic axis (EA) (see Figure 2). Both our computational fluid dynamics (CFD) and computational structural dynamics (CSD) models are considered low-fidelity.

The theoretical fluid model ignores gravity, viscosity, and flow compressibility effects. The hydrofoil is assumed to be deeply submerged, so free-surface and wave orbital velocity effects on the loads are negligible. We justify neglecting gravity because the weight of the foil compared to dynamic pressure loads at our speeds (>10 m/s) is an order of magnitude smaller and because we later use a surrogate load for gravity waves when we apply wave loading. We ignore viscosity in the model because we limit our computations to avoid flow regimes where viscous effects like flow separation are present. The model neglects multiphase compressibility effects because we use a surrogate model for the loading due to small partial cavity shedding dominated by re-entrant jet dynamics. We ignore free-surface effects because the depth-to-chord ratios we investigate (about 3.7) are high enough. The free-surface effects on the lift are relatively invariant with respect to varying depth-based Froude number [34].

2.1.1 Governing equations

Diagrams of the model are given in Figures 1 and 2. The vertical direction is the z -axis, the spanwise direction is the y -axis, and the flow direction is the x -axis; the origin is at the root mid-chord of the hydrofoil, where b is the semi-chord. Primes denote the rotated axes aligned with Λ , shown in the planform view in Figure 2. The single equivalent fiber angle (θ_f) is defined relative to the y' -axis and is positive when fibers are oriented towards the leading edge. While real composites have multiple laminae, it is possible to use a single equivalent fiber orientation representing the load-dependent deformation of a multi-layered composite with bend-twist coupling as was shown by Young et al. [35]; however, a multi-layer model should eventually be used if the goal is to capture interlaminar stresses and perform a final structural integrity analysis. In practical applications, one can use a model to obtain the single equivalent layer to generate a real composite layup of many plies that minimizes the differences in load-dependent bend-twist structural parameters between the real, multi-layered, and the equivalent single-layered structure [35]. The static hydrodynamic arm (eb) is the dimensional distance from the EA to the center of pressure (CP), where positive is when the CP is forward of EA. The dimensional distance (ab) is from the EA to the

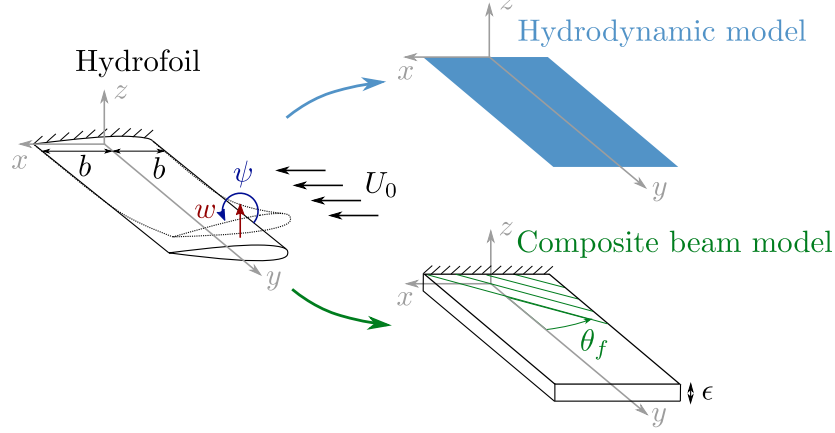


Figure 1: Diagram of composite hydrofoil beam model where z is the vertical direction. The hydrofoil is modeled as a thin airfoil for the hydrodynamics and as a beam for the structure

mid-chord and is positive if the mid-chord is forward of the EA. The static imbalance arm ($x_\alpha b$) is from the EA to the center of gravity (CG) and is positive when the CG is aft of the EA.

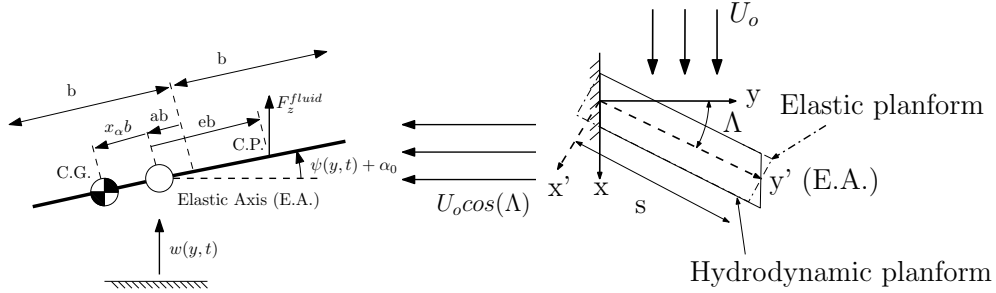


Figure 2: Hydrofoil cross-section (left) at a given spanwise slice with arrows denoting positive conventions and planform (right) showing the sweep variable

The governing differential equations describing the composite beam's spanwise bending and twisting deformations are

$$EI_s w^{iv} + abEI_s \psi^{iv} + K_s \psi''' + m_s \ddot{w} - m_s x_\alpha b \ddot{\psi} = F_z^{\text{ext}} \quad (1)$$

$$abEI_s w^{iv} - K_s w''' + S_s \psi^{iv} - GJ_s \psi'' + I_s^{EA} \ddot{\psi} - m_s x_\alpha b \ddot{w} = M_y^{\text{ext}}, \quad (2)$$

which are two fourth-order, nonlinear partial differential equations (PDE). We use Newton's and Lagrange's notations for time and space derivatives, respectively. There are eight mixed-type boundary conditions for the PDE's given in A: four that describe the clamped root and four that describe the shear and moments at the free tip. The spanwise terms EI_s , GJ_s , K_s , and S_s are bending stiffness, torsion stiffness, bend-twist coupling stiffness, and structural warping resistance, respectively. These parameters can vary with spanwise location if the geometry of the cross-sections changes along the span. Equations (1) and (2) were derived through virtual work and energy principles as

shown by Lottati [36]. Akcabay and Young [20] provide the constitutive relations that relate equivalent fiber angle (θ_f) to EI_s , GJ_s , and K_s . Euler-Bernoulli beam theory assumes plane sections remain plane (no shear effects) and deformations remain small, which is sufficient for modeling low-order modes for hydrofoils; we additionally consider structural warping because warping effects are more significant for low geometric AR structures [20], where $AR = s/\bar{c}$ is the ratio of the span (s) to the mean chord (\bar{c}). Akcabay and Young [20] have shown that for marine lifting bodies with lower aspect ratios compared to aircraft structures, warping resistance (S_s) effects were important in the predicted natural frequencies and stability boundaries because they scale with $1/s^4$. Warping resistance resulted in higher natural frequencies and stability boundaries than classical beam theory.

The unsteady fluid loads and any other external loads are accounted for in the right-hand side as F_z^{ext} and M_y^{ext} . The sectional fluid loading is in the form

$$\begin{Bmatrix} F_z^{\text{fluid}} \\ M_y^{\text{fluid}} \end{Bmatrix} = -(\mathbf{M}_f \ddot{\mathbf{q}} + \mathbf{C}_f \dot{\mathbf{q}} + \mathbf{K}_f \mathbf{q}) \quad (3)$$

where the generalized coordinate vector is

$$\mathbf{q}(y) = \begin{Bmatrix} w(y) \\ \psi(y) \end{Bmatrix}, \quad (4)$$

and the fluid inertial (\mathbf{M}_f), damping (\mathbf{C}_f), and stiffness (\mathbf{K}_f) matrices are

$$\mathbf{M}_f = \pi \rho_f b^2 \begin{bmatrix} 1 & ab \\ ab & b^2 (\frac{1}{8} + a^2) \end{bmatrix} \quad (5)$$

$$\mathbf{C}_f = \frac{1}{2} \rho_f b U_0 \begin{pmatrix} \cos(\Lambda) \begin{bmatrix} a_0 2C(k) & -b [2\pi + a_0(1 - 2a)C(k)] \\ a_0 eb 2C(k) & \frac{b}{2}(1 - 2a)(2\pi b - a_0 2ebC(k)) \end{bmatrix} + \\ \sin(\Lambda) \frac{\partial}{\partial y} \begin{bmatrix} 2\pi b & 2\pi ab^2 \\ 2\pi ab^2 & 2\pi b^3 (\frac{1}{8} + a^2) \end{bmatrix} \end{pmatrix} \quad (6)$$

$$\mathbf{K}_f = \frac{1}{2} \rho_f U_0^2 \cos(\Lambda) \begin{pmatrix} \cos(\Lambda) \begin{bmatrix} 0 & -C(k) 2ba_0 \\ 0 & -2eb^2 a_0 C(k) \end{bmatrix} + \\ \sin(\Lambda) b \frac{\partial}{\partial y} \begin{bmatrix} a_0 2C(k) & -a_0 b(1 - 2a)C(k) \\ 2eba_0 C(k) & \pi b^2 - a_0 eb^2(1 - 2a)C(k) \end{bmatrix} \end{pmatrix} \quad (7)$$

where U_0 is the flow speed, and ρ_f is the fluid density.

The fluid equations are derived from Theodorsen's unsteady airfoil potential flow theory extended to 3D with corrections for sweep and spanwise effects [37–40]. Theodorsen hydrodynamics assumes sections are thin, symmetric airfoils with fully attached and fully wetted flow undergoing small amplitude harmonic motion. The vortices are assumed to be shed into the wake at the three-quarter chord position. This theory is appropriate for capturing added mass, fluid damping, and fluid de-stiffening loads for our model since we consider cases with a very small partial cavity, where the effect

of the cavity on the added mass, damping and fluid disturbing forces are negligible. For flow regimes with a much larger partial cavity or a supercavity, the added mass and damping can be modified following the relations as a function of the effective cavitation number given by Harwood et al. [9] and Young et al. [33]. Theodorsen's function is $C(k) = H_1^2(k) / [H_1^2(k) + jH_0^2(k)]$, which is a function of the reduced frequency, $k = \omega b / (U_0 \cos(\Lambda))$. We use $j = \sqrt{-1}$. Theodorsen's function is a complex, nonlinear function consisting of Bessel functions of the third kind (a.k.a. Hankel functions) that models the influence of memory effects (induced circulation) of the body's wake vorticity on the quasi-steady loads, which we define as damping and stiffness, in the frequency domain. The zero-frequency limit is when oscillation frequency (ω) is low, when the speed (U_0) is high, or both. Low values for the reduced frequency k lead to $\Re\{C(k)\} \rightarrow 1$ and $\Im\{C(k)\} \rightarrow 0$, which is the same as steady (a.k.a. static) hydroelastic performance. For the infinite-frequency limit or high k (highly unsteady motion), $\Re\{C(k)\} \rightarrow 1/2$ and $\Im\{C(k)\} \rightarrow 0$. The component $\Re\{C(k)\}$ reduces the magnitude of the terms containing $C(k)$ within the fluid damping and de-stiffening loads; the imaginary component causes phase shifts for those terms. The non-dimensional sectional lift slope (a_0) is calculated using Glauert's lifting line theory (LLT) to account for 3D effects [32]. LLT is less accurate for low AR bodies, but since our geometry has the wall condition, the effective AR ($AR_e = 2s/\bar{c}$) is twice the geometric AR. Liao et al. [41] showed that when the AR_e is about 6.7, which is what we use later, the spanwise lift distribution from 3D Reynolds-averaged Navier Stokes simulation is nearly elliptical, so LLT is sufficiently accurate for our study.

Positive terms in the fluid equations (5)–(7) are restoring forces while negative signs are disturbing. Deviatoric terms in all matrices are nonzero, which means that in addition to coupling due to material anisotropy, the fluid equations are coupled in the DOF's. Also, damping and fluid stiffness terms are proportional to U_0 and U_0^2 , respectively, so the relative importance of these fluid effects grows with increasing speed. The quasi-steady terms also change with oscillation frequency because of $C(k)$. Fluid inertial, damping, and stiffness forces depend on fluid density (ρ_f), which is much greater than in air. Hence, the in-water natural frequencies of the hydrofoil are much lower than in-air natural frequencies because of greater total system mass. Furthermore, the in-water natural frequencies decrease with speed since total system stiffness decreases because of greater fluid de-stiffening or disturbing forces. The negative $C_{f,12}$ and $K_{f,12}$ fluid terms in Equations (6) and (7), respectively are responsible for coupled mode flutter of the low-frequency 'new mode' at sufficiently high speeds. This is discussed more in Section 4.

2.1.2 Solution method

We assume a solution of the form

$$\mathbf{q} = \tilde{\mathbf{q}}e^{pt} \quad (8)$$

where the eigenvalue is $p = \xi + j\Omega$, and the tilde indicates complex amplitude; $\xi > 0$ is instability because there is negative damping, and Ω is the system natural frequency. The total damping loss factor (energy dissipated per cycle) is $\eta_t = -2\xi/\Omega$. The governing PDE's are recast as state-space vectors, and the system of eight first-order,

ordinary differential equations (ODE) along with the boundary conditions are solved with an explicit, 4-stage Runge–Kutta (RK) method.

We solve the boundary value problem (BVP) to get the static and dynamic response in the frequency domain. The static and dynamic response are broken up as $\mathbf{q}(y) = \mathbf{q}_{\text{stat}}(y) + \mathbf{q}_{\text{dyn}}(y)$. The term $\mathbf{q}_{\text{stat}}(y) = [w_{\text{stat}}(y), \psi_{\text{stat}}(y) + \alpha_0]^T$ includes the initial angle of attack. The static case solves $(\mathbf{K}_s + \mathbf{K}_f) \mathbf{q}_{\text{stat}} = 0$ for the spanwise static deformations where we set $C(k) = 1$ in \mathbf{K}_f ; matrix \mathbf{K}_s comes from setting time derivative terms in Equations (1) and (2) to zero. The dynamic case solves the governing equations for the complex amplitude of the fluctuating, spanwise deformations ($\tilde{\mathbf{q}}_{\text{dyn}}$) with an external force and moment of prescribed amplitude and frequency. Sweeping over ω and computing $|\tilde{\mathbf{q}}_{\text{dyn}}|$ gives us the frequency response spectra of the hydrofoil.

We perform modal analysis using the iterative p - k method described by Beaulieu and Noiseux [42], which can compute the first six modes of the cantilevered hydrofoil. It employs a shooting method on the governing PDE’s and boundary conditions and a residual minimization to converge on the eigenvalues (p). The system eigenvalues represent the poles of an n^{th} -order system transfer function with variable, open-loop gain, where n is the number of modes and the variable input is U_0 .

2.2 Design problem

An optimal composite hydrofoil design would meet all steady lift or moment requirements while avoiding or delaying cavitation, separation, and ventilation. The design should also avoid material failure modes, excessive vibrations, fatigue, dynamic load amplification, and instability. A suboptimal hydrofoil can harm the vessel’s safety, controllability, and efficiency.

We are concerned with a preliminary design problem where we wish to rule out the worst design configurations in a large initial design space, hence the use of low-fidelity tools. The qualitative sample design problem is described in Table 1; we further define the mathematical form for these terms in Section 2.3.

In a later detail design phase, one would use a higher fidelity tool such as presented in Garg et al. [3] and Liao et al. [21] to consider detailed effects such as cavitation, separation, and ventilation avoidance, composite material failure mechanisms, drag minimization through structural and shape optimization. For example, the complete design problem may look like Table 1 but with additional constraints to avoid or delay cavitation, separation, and ventilation and to avoid composite material failure initialization.

2.3 Mathematical form of objectives and constraints

This portion only covers mathematical formulations of objectives and constraints from the design problem (1) that are less intuitive; for example, the steady lift constraint is not explained because it is a straightforward equality constraint. Additionally, we devise functions with continuity and differentiability in mind for future work.

The dynamic FSI of a lifting surface we are concerned about are the system eigenvalues (p) and the frequency response curves. Superscript $*$ denotes non-dimensional

Table 1: Preliminary design problem for a composite hydrofoil. Later designs would consider high-fidelity flow and structural performance

minimize	overall vibrations
with respect to	geometric and material variables
subject to	steady lift requirements for design points
	steady and dynamic tip deflections constraint
	constraints on the maximum amplitude deformations of the spanwise averaged frequency response
	avoid critical frequencies tabulated in Table 7 (wave encounter frequency, rigid body resonance, impeller blade and shaft rates, engine excitation, small partial cavity shedding frequency)
	avoid modal coalescence

quantity, and we non-dimensionalize using the characteristic length and frequency in Table 2. We use gravitational acceleration (g) to non-dimensionalize variables because although our model currently neglects gravitational effects, Froude-scaling is typically used in naval applications [10].

Table 2: Characteristic parameters for non-dimensionalization. We only need the mean semi-chord (\bar{b}) and acceleration due to gravity (g) as simple known constants

Variable	Units	Characteristic parameter
Length	m	\bar{b}
Frequency	Hz	$\omega_c = \sqrt{\frac{g}{\bar{b}}}$

The objective function to capture overall vibrations from Table 1 should consider deformations over the whole spatial domain and spectral loads for the various operating conditions. We devise the merit function for each operating point as

$$f_{\text{vib}} = \sum_{\text{nDOF}} \left(\int \bar{\mathbf{q}}_{\text{dyn}}^*(\omega) \frac{\omega}{\omega_c^2} d\omega \right), \quad (9)$$

and it is computed using numerical integration where $\bar{\mathbf{q}}_{\text{dyn}}^*(\omega)$ is the non-dimensional dynamic deformation frequency response spectrum averaged over the span for bending and twisting. As such, there is one $\bar{\mathbf{q}}_{\text{dyn}}^*(\omega)$ curve for bending and one for twisting. We weight by non-dimensional frequency because this promotes designs with better fatigue characteristics since high-amplitude, high-frequency deflections lead to accelerated fatigue.

Consider a hypothetical $\bar{\mathbf{q}}_{\text{dyn}}^*(\omega)$ given for bending in Figure 3 resulting from different sources of external harmonic loads. We use a toy example that includes wave excitation and re-entrant jet-driven partial cavity shedding to illustrate what the objective means with respect to a response spectrum. The objective function represents the non-dimensional area under this curve weighted by the non-dimensional frequency. We can see that trying to minimize f_{vib} for all elastic DOF's would favor designs that have

shorter, narrower peaks with lower frequency in the response, which may be undesired.

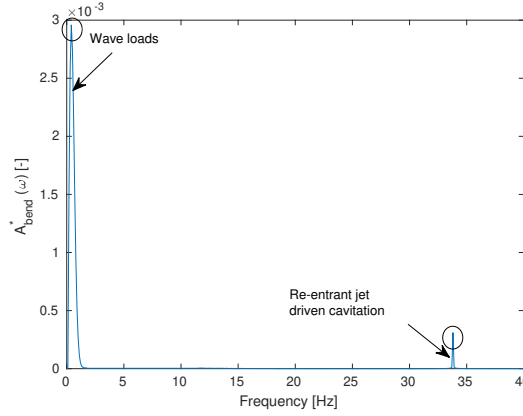


Figure 3: Hypothetical frequency response spectrum for the bending DOF of an unswept carbon fiber-reinforced plastic (CFRP) hydrofoil due to separate external sources of excitation. Wave loading computed assuming simple Rayleigh distribution, and cavitation loading computed using semi-empirical models from Young et al. [33]. This is not the actual load spectrum on our hydrofoil; the purpose is to visually explain how heights and widths of peaks in the dynamic response can be influenced by external excitations and should be considered in a merit function

We use two separate constraints to limit excessive steady and dynamic tip deflections because the most significant deformations are typically at the tip. There is one constraint value for each DOF, so there are four in total that would be applied on the flow condition with the highest loading. For steady tip deflections, we use

$$h_{\text{tip, stat}, i} = \mathbf{q}_{\text{stat, tip}, i}^* - \mathbf{q}_{\text{stat, crit}, i}^* \leq 0 \quad \text{for } i = 1, 2 \quad (10)$$

where $\mathbf{q}_{\text{stat, tip}}^* = [w_{\text{stat, tip}}/\bar{b}, \psi_{\text{stat, tip}} + \alpha_0]^T$ is the non-dimensionalized static tip values.

We define $\mathbf{q}_{\text{tip}}^*(\omega) = \mathbf{q}_{\text{dyn, tip}}^*(\omega) + \mathbf{q}_{\text{stat, tip}}^*$ as the non-dimensional total (dynamic plus static) tip deflection vector. The term $\mathbf{q}_{\text{crit}}^*$ is the user-prescribed bound that should not be exceeded based on design requirements. To consider dynamic tip deflections, we compute the tip values in the total deformation response spectra because the total tip deflection (mean plus fluctuating plus initial rigid angle) influences the stall or material failure characteristics. We take the maximum value from the tip frequency response spectra. The total (dynamic, static, and rigid) tip deformation constraint is

$$h_{\text{tip}, i} = \mathbf{q}_{\text{tip}, i}^* - \mathbf{q}_{\text{crit}, i}^* \leq 0 \quad \text{for } i = 1, 2 \quad (11)$$

so $\mathbf{q}_{\text{tip}}^* = [w_{\text{tip}}/\bar{b}, \psi_{\text{tip}}]^T$ is the non-dimensionalized total tip deformation values. For this study, we simplify matters by using $\mathbf{q}_{\text{crit}}^* = \mathbf{q}_{\text{stat, crit}}^* = [0.5, 10^\circ]^T$ to avoid excessive deflection and tip stall (bending below 25% of mean chord and total geometric tip angle less than 10°). Since $\mathbf{q}_{\text{tip, dyn}}^*$ is always positive since we take the magnitude, the steady tip deflection constraint will not be active unless there are no tip vibrations, but it could be tightened in future work to be more conservative.

We also want to limit the maximum amplitude of spatial domain-averaged dynamic deformations. We devised a constraint to limit the maximum amplitude deformations in the frequency response given as

$$h_{\text{def},i} = \bar{\mathbf{q}}_{\text{dyn}_i}^* - \bar{\mathbf{q}}_{\text{dyn}_{\text{crit},i}}^* \leq 0 \quad \text{for } i = 1, 2 \quad (12)$$

and it is computed using a max function over the frequency range. We use critical mean dynamic deformations as $\bar{\mathbf{q}}_{\text{dyn}_{\text{crit}}}^* = [0.3, 5^\circ]^T$ to avoid excessive average dynamic bending (below 15% of mean chord) and dynamic twisting, respectively.

We use two constraints on the system's eigenvalues to avoid modal coalescence and lock-in or resonance with critical frequencies. These constraints are applied to the wetted values, not in vacuo values.

The frequency coalescence constraint limits the minimum frequency band gap between adjacent modes to avoid modal coalescence. The indicator function is

$$I_n^{(g)} = (0.15)^2 - \left(1 - \frac{\omega_{n+1}}{\omega_n}\right)^2 \leq 0 \quad n = 1, 2, \dots, N-1 \quad (13)$$

where only the eigenvalues of the modes evaluated (user prescribed number N) are used. The superscript (g) denotes the indicator function is for the band gap.

This constraint tells us that if the next highest modal frequency is within 15% of the previous modal frequency, the constraint is violated. We use 15% to consider both the uncertainty and variability in the low-fidelity modeled frequencies without being overly restrictive; frequencies (both hydrofoil resonance and external) will likely fluctuate in actual operation due to changing flow speeds, vessel motions, and engine revolutions per minute (RPM). Ideally, all modes would be evaluated because damping decreases for higher modes, but the algorithm and cost preclude this. The denominator could be zero in the case of static divergence, but designs with static divergence are removed since the static limit constraint prevents this. Therefore, this formulation is valid provided it is used in conjunction with the rest of the optimization algorithm.

The indicator function $(I^{(g)})$ in Equation (13) is aggregated for the $N-1$ frequency band gaps using the Kresselmeier–Steinhauser (KS) function shown in Equation (14) over the modes evaluated, where ρ_{KS} is the aggregation parameter where higher values approach the actual constraint. In all formulations, our default is $\rho_{\text{KS}} = 80$. Squaring the frequency term in Equation (13) bastions against mode hopping or reordering to ensure the output is of the correct sign. It also keeps the derivative continuous, unlike an absolute value function. Mode hopping is a numerical side effect of the iterative solver that can occur if eigenvalues are close to each other in frequency. The benefit of the KS function is that it acts like a soft maximum function and is therefore suitable for gradient-based optimization [43, Sec. 5.7]. The following formulation is the finite-set constraint formulation to avoid overflow due to large powers of e , making it appropriate for finite-precision arithmetic [44]. The final constraint is

$$h_g = \text{KS} (I_n^{(g)}) = \max_n (I_n^{(g)}) + \frac{1}{\rho_{\text{KS}}} \ln \left(\sum_{n=1}^{N-1} e^{\rho_{\text{KS}} (I_n^{(g)} - \max_n (I_n^{(g)}))} \right) \leq 0. \quad (14)$$

The frequency avoidance constraint considers the band gap between modal and external excitations. Examples of external excitations include engine speed and waves. This constraint is useful when a designer cannot access the excitation spectrum, only the peak frequency. The indicator function has a similar formulation to $I^{(g)}$ in Equation (13). A two-level KS aggregation is employed. The first level is over all the modal frequencies, captured by

$$I_{n,k}^{(l)} = (0.15)^2 - \left(1 - \frac{\omega_n}{\omega_{exc,k}}\right)^2 \leq 0 \quad n = 1, 2, \dots, N, \quad (15)$$

where superscript (l) denotes the indicator is related to avoiding lock-in. A weakness of this constraint is it does not directly consider the effect of foil flexibility on the lock-in region even though it has been shown that increasing flexibility (quantified by the reduced velocity $\bar{U} = U/(\Omega_\psi b)$ where Ω_ψ is the first in-air twisting natural frequency) has increased lock-in susceptibility [16, 45]; Once again, this constraint limits the modal frequency to be outside of 15% of the external. Then we evaluate the second level

$$f_k = \max_n(I_{n,k}^{(l)}) + \frac{1}{\rho_{KS}} \ln \left(\sum_{n=1}^N e^{\rho_{KS}(I_{n,k}^{(l)} - \max_n(I_{n,k}^{(l)}))} \right) \quad k = 1, 2, \dots, K \quad (16)$$

over all the excitation frequencies of interest and aggregate once more to give the final constraint inequality as

$$h_l = \max_k(f_k) + \frac{1}{\rho_{KS}} \ln \left(\sum_{k=1}^K e^{\rho_{KS}(f_k - \max_k(f_k))} \right) \leq 0. \quad (17)$$

The flutter constraint we use is from Jonsson et al. [30], which uses double KS aggregation on $\Re\{p\}$: first for all dynamic pressures ($q = 1, \dots, N_q$), and then for all evaluated modes ($n = 1, \dots, N$). The result is the single constraint

$$h_{\text{flut}} = \text{KS}(\text{KS}(\Re\{p_{n,q}\})) \leq 0, \quad (18)$$

which is a conservative constraint on flutter because linearized theory typically has a more conservative instability speed prediction than if all nonlinear flow and structural effects are considered (limit-cycle oscillation happens after flutter).

3 Design optimization setup

3.1 Baseline design

We apply the optimization algorithm to a full-scale prototype CFRP lifting surface that could be the horizontal part of a rudder T-foil on a medium-sized, surface craft, with a full-scale vessel length of 20 m (assuming draft of 0.3 m). We model one half of the T-foil's lifting surface as a cantilevered beam. For context, this is around the length of the USS Flagstaff owned by the US Coast Guard in the 1960's (shown in Figure 4). We assume that the vessel has two foils in the conventional configuration

with about 20% of the weight on the rear foil. We obtain the lifting surface planform area by starting with a 2% profile area approximation and iterating geometries until the lift coefficient for the lowest foilborne speed is reasonable ($C_L = 0.6$). We use values from Zubaly [46] to determine the other vessel particulars tabulated in Table 3.



Figure 4: USS Flagstaff was a 25 m LOA foiling vessel from the 1960’s. Our hypothetical design is for a composite lifting surface of a T-foil for a similarly sized vessel.

While we could easily simulate the full-scale hydrofoil, we want results that can be reproduced in experiments. The baseline scaled model studied in this section is a 1/3 length-scale, zero sweep and zero fiber angle foil that could be tested in a cavitation tunnel. We use Froude (Fn) scaling because a smaller model of the vessel with the foil can run at lower speeds; because the governing equations neglect gravitational effects, Froude scaling is simply a method to scale the inflow velocity to the foil. To obtain the perfectly scaled parameters, we use the scaling table derived for flexible marine composite foils by Ng et al. [10] shown in Table 4; these scaling laws apply to flexible composite lifting surfaces in potential flow and any lifting surface model of lower order governing physics. The scaling laws for flexible anisotropic materials are more stringent than those for isotropic or effectively rigid materials. This is because more parameters in the flexible composite governing equations (such as those related to bend-twist coupling) lead to more non-dimensional Π terms that must be kept equal based on the Buckingham Π theorem. The scaling notation is $\lambda_\phi = \phi_m/\phi_p$, where ϕ is some parameter of interest for the model (subscript m) or prototype (subscript p).

3.2 Operating conditions

The full-scale vessel operates in head seas where we assume foilborne operating speeds between 15–20 m/s (30–39 kts) for the full-scale, with 25% probability of operation on the 15 m/s takeoff speed and 75% on the 20 m/s cruising speed. The probability of operation are the weights for the objective functions for each operating point, and we chose them, assuming a foiling vessel should spend most of its time foiling. These design points and their weights are summarized in Table 5, where cavitation number is $\sigma = (p_\infty - p_v) / (0.5\rho_f U_0^2)$. We calculate σ using a vapor pressure of $p_v = 2.33$ kPa. Ideally, a probability density function would be used to weight the speed envelope,

Table 3: Vessel particulars of full scale and model. We simulate a model scale so results could be validated in an experiment

Parameter	Full-scale	Model ($\lambda_L = 1/3$)	Units
Length overall, LOA	20	6.7	m
Length-to-beam ratio, LOA/B	6	6	—
Design draft, T	0.3	0.1	m
Waterplane coefficient, C_{WP}	0.7	0.7	—
Block coefficient, C_B	0.4	0.4	—
Foil depth	1	0.3	m
Vessel weight	8	0.3	tonne

Table 4: Scaling factors using Froude scaling ($\lambda_{Fn} = \lambda_{U_0}/\sqrt{\lambda_g \lambda_L} = 1$) for geometrically similar composite plates assuming same fluid medium and gravitational constant. Meeting every scaling factor here satisfies complete similitude between model and prototype for the low-fidelity composite hydrofoil model [10].

Parameter	Symbol	Expression	Fn scale
Froude number	$Fn = \frac{U_0}{\sqrt{gb}}$	λ_{Fn}	1
Solid density	ρ_s	λ_{ρ_s}	1
Poisson’s ratio	ν_{ij}	$\lambda_{\nu_{ij}}$	1
Semi-chord	b	λ_L	λ_L
Inflow velocity	U_0	λ_{U_0}	$\lambda_L^{1/2}$
Elastic moduli	E_{ij}	$\lambda_{E_{ij}}$	λ_L
Shear moduli	G_{ij}	$\lambda_{G_{ij}}$	λ_L
Natural, response, forcing frequencies and frequency resolutions	ω	λ_ω	$\lambda_L^{-1/2}$

but Liem et al. [47] showed for aircraft that as long as the important design points are considered, the optimized solution does not change much with respect to the sheer number of design points; they showed a small drag reduction at the nominal condition between one design point and five design point optimization. Their multipoint design still performed better away from the nominal condition, demonstrating the importance of considering at least a few relevant design conditions.

We use incident wave periods with $\omega_{\text{wave}}^{-1} = 8$ s where we compute wave encounter frequency (ω_e) from

$$\omega_e = \omega_{\text{wave}} \left(1 - U_0 \frac{\omega_{\text{wave}}}{g} \cos(\beta) \right), \quad (19)$$

with $\beta = 180^\circ$ for head seas. We then assume a Rayleigh-distributed spectrum following $\zeta(\omega) = \frac{\omega}{\omega_e} e^{-\left(\frac{\omega^2}{\omega_e^2}\right)}$ where the scale parameter ω_e is the wave encounter frequency. We assume World Meteorological Organization (WMO) Sea State 3 (calmer end of moderate waves) conditions with wave amplitude $A_w = 0.5$ m, so the amplitude spectrum

Table 5: Two discrete design operating points are considered. Foil depth for the scaled model would be 1/3 of the full-scale, so to scale σ , the ambient pressure must be lowered from typical 101.3kPa to 9.97kPa for the $U_0 = 10$ m/s case and to 105.51kPa for the $U_0 = 15$ m/s case.

Variable	Units	Full-scale	Model ($\lambda_L = 1/3$)
Takeoff (weight = 25%)			
U_0	m/s	10	5.8
Cavitation number	—	2.2	2.2
Lift coefficient (C_L)	—	0.6	0.6
Cruise (weight = 75%)			
U_0	m/s	15	8.7
Cavitation number	—	0.97	0.97
Lift coefficient (C_L)	—	0.3	0.3

becomes $A(\omega) = \zeta(\omega)A_w$, which tells us the amplitudes of waves at that excitation frequency. We compute the amplitude of wave loads on a single submerged hydrofoil using

$$\tilde{F}_{\text{wave}}(\omega) = \pi \rho_f s \bar{c} A(\omega) e^{-k_{\text{wave}} h} \left| j \frac{1}{4} c \omega_{\text{wave}} \omega_e + \omega_{\text{wave}} U_0 C(k) \right| \quad (20)$$

which was originally derived by Faltinsen [34] based on potential flow with depth effects. We simplified the equation by ignoring vessel motions. In this equation, $k = 0.5 \omega_e c / U_0$ is wave reduced frequency, h is the depth of the foil from the free surface, and $k_{\text{wave}} = \omega_{\text{wave}}^2 / g$ is the wave number. Interactions with the free surface are not considered in this equation. For simplicity, we assume the wave moments are related to the forces by $\tilde{M}_{\text{wave}} = \tilde{F}_{\text{wave}} e b$. The full-scale wave spectrum is Figure 5, and we can see that the wave frequency does not change much between flow speeds.

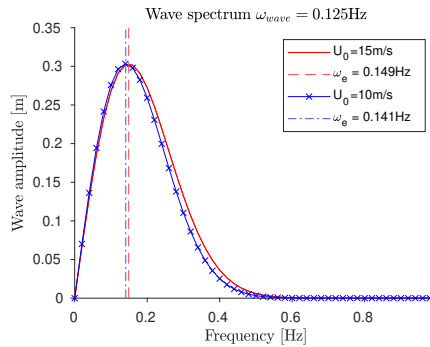


Figure 5: Rayleigh distributed full-scale wave spectrum in head seas. Peak frequency does not differ much between the two speeds

Finally, we scale all geometric, material, fluid, and loading parameters required by the computational model according to Fn -scaling to obtain the model-scale lifting surface in the rightmost column of Table 6. The model must have particular material properties to scale steady and dynamic FSI, and a general polymer matrix

composite (PMC) can be made according to these specifications. Tuning the exact solid density may be difficult, which one can verify from material selection diagrams (Ashby plots [48]). Also, in reality, scaling of marine composites is not straightforward if higher fidelity physics such as ply scaling, material failure, or water absorption, for example, are included [10, 49, 50], so this scaling does make simplifying assumptions about the modeled physics.

Table 6: Baseline and model parameters of the full-scale and model hydrofoil assuming a perfectly Froude-scaled model. Lines separate geometric, fluid, and material parameters. The 1, 2, and 3 directions represent the Cartesian coordinates defined perpendicular to the fiber axis (2 is along the fiber direction in Figure 1).

Variable	Units	Full-scale	Model ($\lambda_L = 1/3$)
s	m	0.9	0.3
$2b$	m	0.27	0.09
Λ	$^\circ$	0	0
$\epsilon/(2b)$	—	6%	6%
$x_\alpha b$	m	0	0
$r_s b$	m	0.078	0.026
eb	m	0.0675	0.0225
ab	m	0	0
ρ_f	kg/m ³	1000	1000
Wave peak frequency ω_{wave}	Hz	0.125	0.2165
WMO sea state 3 wave amplitudes, A_w	m	0.5	0.1667
Submergence depth, h	m	1	0.33
Material	—	CFRP	PMC
θ_f	$^\circ$	0	0
ρ_s	kg/m ³	1590	1590
$E_1 = E_3$	GPa	13.40	4.47
E_2	GPa	117.80	39.3
$G_{12} = G_{23}$	GPa	3.90	1.3
ν_{23}	—	0.25	0.25

3.3 Critical frequencies

3.3.1 Cavitation

For simplicity, we set cavity shedding as a frequency constraint rather than as load spectra. While the general objective in designing high-speed lifting surfaces would be to avoid cavitation, small amounts of partial leading edge or tip vortex cavitation may develop at the highest speeds. We determine frequencies using semi-empirical models devised for a flexible CFRP hydrofoil [33, 51, 52]. The 1/3 scaled model is similar in geometry to the NACA0009 studied in their work but with no taper. Semi-empirical equations from Young et al. [33] predict peak frequencies due to cavity shedding based on the effective cavitation parameter.

The mean effective cavitation parameter is defined as $\psi_e = \sigma/(2\alpha_e)$ where $\alpha_e = \bar{\psi} + \alpha_0$ is the effective angle of attack. However, we will find ψ_e by prescribing a cavity length-to-chord ratio (L_c/c) and using the relation

$$L_c/c = 2.3e^{-0.35\psi_e}, \quad (21)$$

which is appropriate because the L_c/c for an optimized hydrofoil should be no more than 5% for small periods of time (see optimized hydrofoil from Liao et al. [21] for the size of a cavitation zone). In the results shown hereafter, we compute cavitation properties using $L_c/c = 0.05$ to determine the significant cavity shedding frequency to avoid. A cavitation-free, optimized geometry is our end goal, so the cavity shedding frequency should reflect what the optimized lifting surface will experience. Steady hydrodynamic loading for this problem is determined by assuming a fully wetted lift slope instead of the modified lift slope due to sustained cavitation because the optimized foil is not supposed to have sustained cavitation. Moreover, due to small L_c/c , we justify the usage of fully wetted added mass and damping.

We find the mean chord-based Strouhal number of Type II re-entrant jet-driven shedding using

$$St_2 = \frac{f_{c2}\bar{c}}{U_0} = 0.0045\psi_e^3 + 0.12. \quad (22)$$

We do not consider Type I shockwave-driven shedding because the finished design should never have such significant cavitation. We also impose the logic to not compute cavitation frequencies if $\sigma > 1.0$ because most optimized hydrofoil designs can operate cavitation free for $\sigma > 1.0$ at their design C_L 's [21].

3.3.2 Vessel motions

We also need rough approximations of the vessel's seakeeping natural frequencies, which we can do using the uncoupled, undamped, approximated equations based on the vessel parameters. They are

$$\omega_{n,\text{heave}} = \sqrt{\frac{C_{33}}{m + A_{33}}} = \sqrt{\frac{\rho_f g A_{WP}}{m + A_{33}}} \quad (23)$$

$$\omega_{n,\text{roll}} = \sqrt{\frac{\Delta G M_T}{I_{xx} + A_{44}}} = \sqrt{\frac{\Delta G M_T}{m k_{xx}^2 + A_{44}}} \quad (24)$$

$$\omega_{n,\text{pitch}} = \sqrt{\frac{\Delta G M_L}{I_{yy} + A_{55}}} = \sqrt{\frac{\Delta G M_L}{m k_{yy}^2 + A_{55}}}, \quad (25)$$

where C_{33} is heave stiffness, A_{ii} are the fluid-added masses in the i^{th} DOF ($3 \equiv \text{heave}$, $4 \equiv \text{roll}$, $5 \equiv \text{pitch}$), m is mass of the vessel, A_{WP} is waterplane area, k_{xx} and k_{yy} are the radii of gyration, $G M_T$ and $G M_L$ are the transverse and longitudinal metacentric heights, respectively, and Δ is the weight of the ship. For heave, A_{33} is on the order of Δ ; for roll, A_{44} is on the order of $0.2I_{xx}$, the roll radius of gyration (k_{xx}) is around 30–40% of B , and the transverse metacentric height varies based on the application, so we assume it to be around $0.05B$; for pitch, A_{55} is about twice I_{yy} , the pitch radius

of gyration (k_{yy}) is around 0.25LOA, and the longitudinal metacentric height is on the order of LOA. These preceding estimates are based on typical values for ships from the ITTC - Recommended Procedures and Guidelines. All full-scale frequencies were estimated between 0.1 and 0.9 Hz. These natural frequencies assume a low Fn , displacement-type vessel, which is not typical of a foilborne vessel. However, for lack of a better theory, these equations give approximations for critical rigid body frequencies for the sample problem to avoid.

3.3.3 Marine propulsion plant

We assume a waterjet-propelled vessel with a diesel engine and an 18-bladed impeller. We use the specifications for the Caterpillar 3406E diesel engine simply because it is an engine that could potentially provide enough power based on similar vessels¹. However, one would conduct a more thorough resistance and propulsion analysis to choose the correct engine. We just need the engine RPM (2200RPM) since we aim to avoid the excitation frequency. We assume a waterjet impeller at a static 1400 shaft RPM based on typical values seen in design pamphlets for various manufacturers²; shaft RPM changes with vessel speed, but we use a fixed value for simplicity. In reality, one would match shaft RPM with the corresponding vessel speed.

We summarize all critical frequencies in Table 7.

Table 7: Critical frequencies to avoid onboard a high-speed composite craft. Frequencies scaled by Froude scaling.

Source	Full-scale [Hz]	Model scale [Hz]
Peak wave encounter frequency	0.141–0.149	0.244–0.258
Roll, pitch, heave natural frequencies, respectively	0.18, 0.25, 0.85	0.31, 0.43, 1.47
Waterjet impeller shaft at 1400RPM	23.3	40.4
Main engine - Caterpillar 3406E	36.7	63.5
18-bladed impeller blade rate	270.0	467.6
Peak cavity shedding frequency	334	578

3.4 Optimization problem formulation

To solve the problem posed in Section 2.2, we have one multipoint-weighted objective function, where design point weights are based on how much operating time is spent at that design condition. We want one type of objective because having multiple objectives introduces the difficulty of determining the appropriate weights for the different objectives [43, Ch. 9]; as such, the single objective is the area under the frequency response curve (f_{vib}), and all the other dynamic performance metrics are constraints. We choose the weighted area under the frequency response as the objective to minimize because the upper-frequency limit may vary based on the problem. It is challenging to prescribe a constrained upper limit on the weighted area under the frequency response

¹teknicraft.com

²marinejetpower.com offers some guidance on waterjet selection

curve if the upper-frequency limit is not scaled consistently between problems. The upper-frequency limit may vary based on the available information. For example, if a spectral excitation signal from an engine manufacturer only goes between 0 and 360 Hz and another excitation signal from another manufacturer has a different range, the designer has to choose the appropriate frequency range.

In contrast, the functions for frequency avoidance and coalescence, maximum tip deflections, maximum mean deflections, and flutter have intuitive and scalable formulations as constraints. There should be a minimum band gap between critical frequencies and an upper limit on the tip and mean deflections. There is less incentive to expand the frequency band gap and minimize deflections further as long as a critical threshold is met.

The optimization problem is detailed in Table 8. We have geometric and material design variables: fiber angle, sweep, and angle of attack. We do not allow negative sweep or fiber angles since they both promote static divergence. Forward sweep leads to geometric nose-up bend-twist coupling because the apparent angle is increased for positive bending, and the CP is farther ahead of the EA. Forward sweep can also catch marine debris, so it is generally not favored for hydrofoils. Aligning fibers towards the trailing edge leads to material nose-up bend-twist coupling since the hydrofoil is stiffer along the fibers. The angle of attack is a variable because we have steady lift constraints to satisfy.

Table 8: Design optimization problem

	Function/Variables	Description	Lower	Upper	Units	Qty
minimize	$\sum_i \text{wt} \times f_{\text{vib}}$	Area under the frequency response, vibrations	—	—	—	1
with respect to	θ_f	Fiber angle	0	30	°	1
	Λ	Sweep angle	0	30	°	1
	α_0	Rigid angle of attack	1	10	°	1
subject to	$C_{L,\text{stat}} - C_{L,i}$	Steady lift coefficient for design point i	0	0	—	1
	ϵ/c	Thickness-to-chord ratio	10%	10%	—	1
	s	Constant semi-span	s_0	s_0	m	1
	c	Constant chord	c_0	c_0	m	1
	$TR = c_{\text{tip}}/c_{\text{root}}$	Constant taper ratio	1	1	—	1
	$h_{\text{tip, stat}}$	Static tip bending is less than 25% of chord and tip twisting is less than 10°	—	0	—	2
	h_{tip}	Total tip bending is less than 25% of chord and tip twisting is less than 10°	—	0	—	2
	h_g	Frequency coalescence constraint	—	0	—	1
	h_l	Frequency avoidance constraint	—	0	—	1
	h_{def}	Maximum amplitude in mean frequency response in bending is less than 15% of chord and in twisting is less than 5°	—	0	—	2
	h_{flut}	No flutter	—	0	—	1

3.5 Optimization method

Because of the associated overhead cost of setting up gradients and the reduced problem dimensionality of this particular problem, we use a heuristic method for tailoring the steady and dynamic hydroelastic performance. This method is sufficient for a preliminary design, but when the number of design variables is large, it is more scalable to use a gradient-based method [53]. First, we run a parameter sweep of fiber and sweep angles using 10° steps (18 total designs $\times 2$ design speeds = 36 full runs of DCfoil) and plot contours of the objective function to assist us in choosing better designs. The order of solvers is always steady, then dynamic hydroelastic analysis. We first perform a steady analysis by letting α_0 vary to satisfy the steady lift requirement while checking the static deflection constraint. During this steady analysis, if the deflection constraint is violated or the steady lift requirement cannot be met within the range of α_0 , we stop execution because the dynamic analysis is more computationally expensive. Only if designs meet steady performance requirements do we complete the dynamic analysis. For our specific example, the steady performance requirement limits the feasible design variables to $0 \leq \Lambda \leq 30^\circ$, $0 \leq \theta_f \leq 30^\circ$, and $\alpha_0 \leq 10^\circ$.

4 Results

To give a better idea of the performance of the scaled composite hydrofoils in the initial design space, we plot the objective function contours of all designs that meet the steady performance requirements in Figure 6. The first two plots are the contours for the two design points, and the third is the weighted sum. These designs were subjected to the wave loading spectra from Figure 5. Not all of these designs may meet the dynamic constraints, but we show all of them just to build intuition on which configurations have small f_{vib} . The minimum in this design space represents the composite hydrofoil with the smallest weighted area under the frequency response curves, which we formulated to indicate the vibration performance.

While the minimum in Figure 6 may have the least vibration, we circle a smaller space of designs in green in Figure 6 to refine the search for the optimal design. In general, submergence effects on the modal coalescence and mode switching characteristics are more severe for higher fiber angles regardless of flow speed because the torsion and bending frequencies converge to each other at high fiber angle [12]. Excessive backward sweep is also undesirable because of the loss in hydrodynamic efficiency due to downwash and upwash effects on the flow field [54] and increased potential for tip vortex cavitation [55]. For these reasons, we circle the smaller design space ($8^\circ \leq \theta_f \leq 22^\circ$ and $5^\circ \leq \Lambda \leq 20^\circ$) that neglects the smaller merit function values of the higher θ_f and Λ designs. The benefit of not using a formal optimization method for tailoring the steady and dynamic performance is that we have more freedom to use design intuition about aspects our computational model does not simulate.

After applying our dynamic constraints and heuristically checking designs, we reach a preliminary optimal design given in Table 9.

The performance comparison to the baseline is separated into steady and dynamic hydroelastic performance. We plot the static tip deformations in Figure 7 to show that

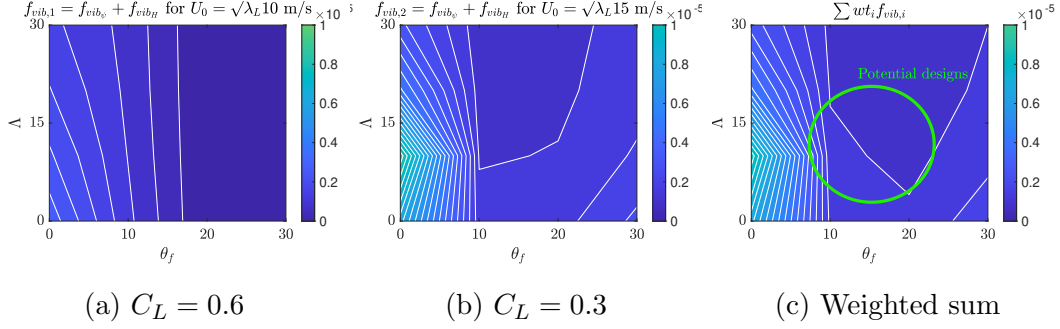


Figure 6: Objective function contours for the PMC 1/3-scaled model hydrofoil in the initial design space before dynamic constraints are applied. Plots 6a and 6b are the separate design speeds and plot 6c is the weighted sum of these based on the design points and probability of operation conditions (weights) given in Table 5. We want to find the design that minimizes the objective (darkest blue contour) to avoid excessive vibrations for our load spectra and satisfy dynamic constraints. The green circle represents a more refined search space based on factors not considered in the model, and white lines are iso-levels for the objective function

Table 9: Optimized versus baseline foil design variables

Variable	Optimized		Baseline	
	$C_L = 0.6$	$C_L = 0.3$	$C_L = 0.6$	$C_L = 0.3$
α_0	8.9°	4.6°	6.1°	1.4°
θ_f	10°		0°	
λ	5°		0°	

the optimized design exhibits smaller static deformations than the baseline because of the nose-down bend-twist coupling caused by both backward sweep and angling fibers towards the leading edge. Figure 7 shows the baseline is close to violating the bending constraint, so the optimized design has better static hydroelastic performance. The steady performance data are tabulated in Table 10. The baseline hydrofoil tip bending and twisting deformations increase with speed because its CP is forward of the EA and has nose-up bend-twist coupling. Because the optimal hydrofoil has a positive sweep and fiber angle, twist deformations are nose-down due to geometric and material nose-down bend-twist coupling. Tip twisting plus the angle of attack remains below 12°, so there is no immediate risk of tip stall. Tip bending is below 25% of the mean chord, so there is no immediate risk of static divergence.

The dynamic hydroelastic performance improvement is shown in Figure 8, where we plot the frequency response spectra of the baseline and optimized designs. The dynamic performance of the foil did not vary significantly between the design speeds, so we show the results for the higher speed for brevity. The baseline’s bending and twisting dynamic response is higher and has more area under the curve, verifying our objective functions. There are no other peaks in the response curves at higher

Table 10: Static wing tip deflections of the baseline and optimized model-scale hydrofoil. Conditions for $C_L = 0.6$ is $U_0 = \sqrt{\lambda_L}10 \text{ m/s} = 5.8 \text{ m/s}$ and for $C_L = 0.3$, $U_0 = \sqrt{\lambda_L}15 \text{ m/s} = 8.7 \text{ m/s}$. Optimized avoids excessive steady deflections and has nose-down tip twist due to both backward sweep and fibers angled towards the leading edge.

DOF	Optimized ($\theta_f = 10^\circ, \Lambda = 5^\circ$)		Baseline ($\theta_f = 0^\circ, \Lambda = 0^\circ$)	
	$C_L = 0.6$	$C_L = 0.3$	$C_L = 0.6$	$C_L = 0.3$
Bending (w/\bar{b})	0.4	0.39	0.42	0.5
Twisting (ψ_{stat})	-0.47°	-0.46°	5.3°	6.3°
Lift coefficient (C_L)	0.27	0.55	0.28	0.57

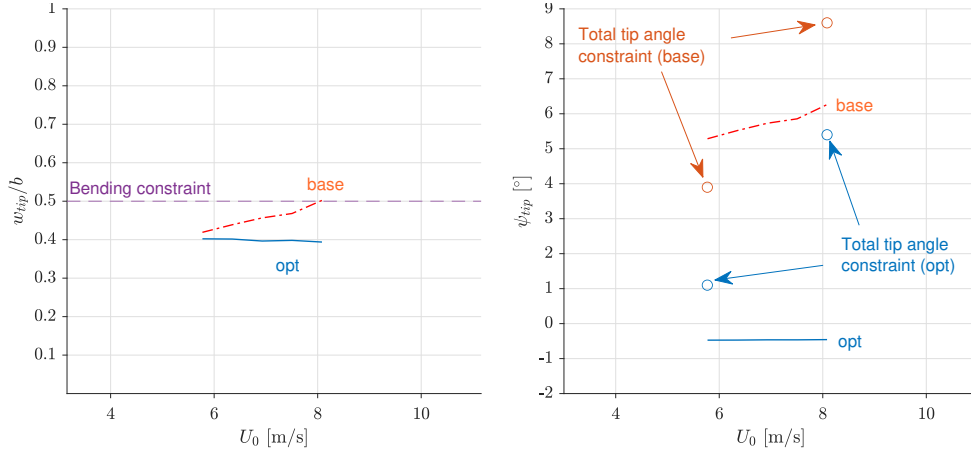


Figure 7: Predicted non-dimensional static tip deformations as a function of speed of the baseline (orange dash-dot) versus optimized (blue solid) design for bending (left) and twisting (right). The optimized design has smaller deformations in the speed range and is well below the bending deflection constraint (horizontal purple dashed line shown on left) and tip angle constraints (color coded open circles shown on right). Tip angle constraints vary with the operating speed because the base angle (α_0) changes with speed to meet the lift requirement.

frequencies since the wave loading is mainly at the lower frequency end, hence the x -axis limits. We also plot the total response of the optimized and baseline result normalized by its static response in Figure 9. Only the higher flow speed is shown for brevity. Peaks denote resonance frequency; the height and width of peaks indicate the level of damping, where higher and skinnier peaks are less damped. Since peaks do not line up with the critical external frequencies, this is further validation that our frequency avoidance constraints worked. The normalized response of the optimized hydrofoil is much lower across all frequencies indicating the foil would have less severe dynamic load amplification. The lower speed case gave a similar conclusion.

We explain the dynamic response behavior in Figure 8 by revisiting the beam

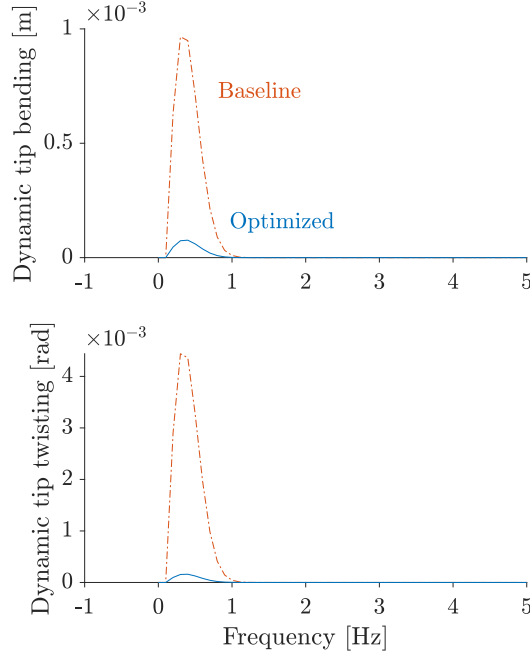


Figure 8: Comparison of dynamic tip deflections between baseline (orange dash-dot) and optimized (blue solid) scaled model clearly show the performance is improved. $U_0 = 8.7 \text{ m/s}$. The optimized design avoids excessive dynamic deformations due to the wave loading spectra

Equations (1) and (2) and the hydrodynamic terms in Equations (6) and (7) where matrix subscript notation is used. The optimized design is stiffer because of both the positive fiber angle and backward sweep. Terms in the \mathbf{C}_f and \mathbf{K}_f matrices with positive signs are restoring, whereas negative signs are disturbing. Nose-down material bend-twist coupling from the fibers is restoring, and backward sweep leads to geometric nose-down bend-twist coupling because of apparent negative camber. The $\sin(\Lambda)$ terms in \mathbf{K}_f are positive except for $K_{f,12}$, so more sweep leads to greater fluid restoring elastic forces. All $\sin(\Lambda)$ terms in \mathbf{C}_f are positive, so more sweep increases the fluid damping forces. The dynamic response of the optimized configuration is lower than the baseline because it is more damped and stiff, and the response is inversely proportional to damping and stiffness.

The final verification and test of the practicality of our design is a root-loci plot for the speed sweep between our given design speeds coupled with mode shape plots. The vessel may have two design speeds, but it will always operate in a range of speeds; transient resonance, while brief, can also lead to excessive vibrations, dynamic load amplification, and accelerated fatigue. We run the steady solver at every speed to determine the α_0 to satisfy the total dimensional lift requirement before using the root-finding solver from DCfoil. The plot of real and imaginary parts of the system poles (a.k.a. the eigenvalues p) is Figure 10.

The mode shapes in quiescent fluid, which can qualitatively describe the mode shape at operating speed since there is no mode switching in this case, are given

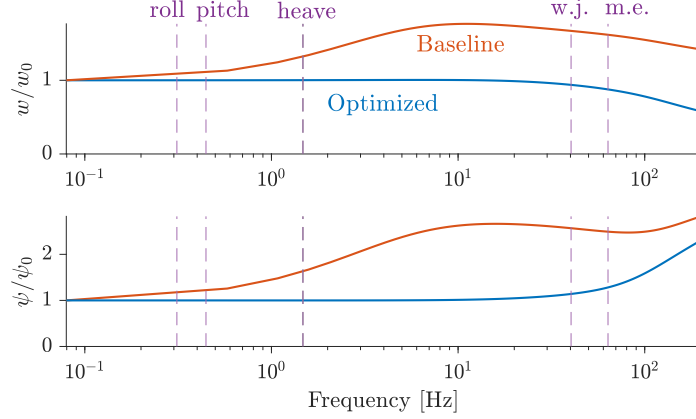


Figure 9: Normalized mean response of optimized vs. baseline scaled model at 8.7 m/s. Critical frequencies marked by dashed purple lines

in Figure 11. They show that the optimized hydrofoil has coupled mode shapes in water due to material anisotropy from the nonzero θ_f ; in comparison, the baseline that has $\theta_f = 0^\circ$ still exhibits some coupling, which is due to the EA and CP not being collocated, but this coupling effect is still less than a case with nonzero θ_f . Sweep does not affect quiescent water mode shapes because it does not affect the quiescent flow field, structural stiffness, or mass distribution. We also see in Figure 11 that the mode order is different because the third mode of the baseline is primarily bending, whereas the optimized has a primarily twisting third mode.

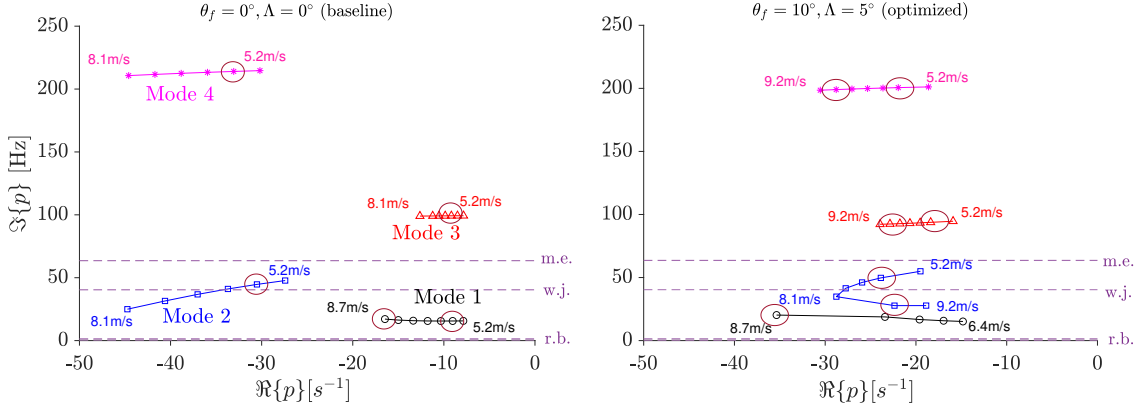


Figure 10: Root-loci of the scaled baseline (left) and optimized (right) composite hydrofoil where critical frequencies to avoid are shown in horizontal dashed purple lines. Due to axis limits, only some of the critical frequencies from Table 7 are shown. The two design points listed in Table 5 are circled in maroon. The baseline design is too close to the waterjet (w.j.) frequency at the low speed so lock-in is a concern. The optimized design has potential transient issues with mode 2's natural frequency passing through the waterjet frequency, but it is still considered a better design than the baseline. There are no issues with the scaled main engine (m.e.) or scaled rigid body (r.b.) frequencies for either configuration.

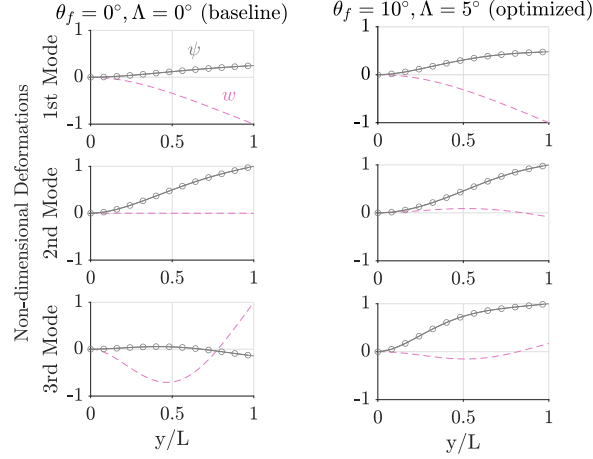


Figure 11: First three non-dimensional mode shapes of the baseline (left) and optimized (right) design in quiescent water (zero flow speed). Compared to the baseline, the nonzero fiber angle of the optimized results in more significant coupling in the bending and twisting mode shapes. The order of modes is also affected by fiber angle (θ_f)

Figure 10 verifies the avoidance of resonance and lock-in of our optimal solution in that the speed-dependent natural frequencies for the design points are far enough from critical frequencies. We also avoid frequency coalescence because the modes' $\Im(p)$ do not converge on each other in this speed range. Flutter is also avoided since the poles do not cross the imaginary axis, but Hopf bifurcation would eventually occur at a higher speed. However, mode 2 (primarily twisting) crosses the waterjet impeller frequency near the full-scale 14 m/s speed, so there will be transient resonance. Fortunately, the system is damped with a damping loss factor of about $\eta_t = 1.65$, so this may not be a severe problem. Most of the damping is due to potential damping from radiated waves captured by Theodorsen's unsteady theory. In reality, there is viscous hydrodynamic damping, but it is ignored because we use potential theory. Structural damping does not play a significant role since it is typically small (we set 2% material damping), whereas hydrodynamic damping can be 10–40% for low-ordered modes.

Equations (1) and (2) and Equations (6) and (7) can once again help explain the system pole behavior in Figure 10. Theodorsen terms with reduced frequency, k have a real and imaginary part related to the magnitude and phase, respectively. Matrices with $\cos(\Lambda)$ are larger in magnitude for small sweep angles compared to those with $\sin(\Lambda)$. Bending-related damping is the first row of terms in \mathbf{C}_f . The term $C_{f,12}$ in the $\cos(\Lambda)$ matrix is always negative for our foil. This term is typically responsible for the bending flutter of the 'new mode' at a high enough speed. All other terms in the \mathbf{C}_f matrix are positive and damp out motions. With this in mind, at any given speed, all these damping effects diminish in magnitude as we approach high frequencies because the real part of Theodorsen's function goes from 1 to 1/2 as $k \rightarrow \infty$; therefore, higher order modes have less damping, which is seen in Figure 10 by the more positive $\Re(p)$ values at higher k .

As speed increases for the optimized foil, $\Im(p)$ in Figure 10 decreases for all modes

since fluid de-stiffening forces and moments increases with U_0^2 . Damping terms in \mathbf{C}_f increase in magnitude with U_0 , which is observed with the $\Re(p)$ values becoming more negative except for mode 2, which is impacted by the speed- and frequency-dependent, negative $C_{f,12}$ term. Since k of mode 2 is decreasing, the negative damping effect of $C_{f,12}$ increases because the bending shape contribution to mode 2 increases with speed. Furthermore, since the structure is anisotropic, the nonzero fiber angle couples bending to twisting deformations, so the negative damping effect of $C_{f,12}$ is more pronounced in the optimized than the baseline because the baseline structurally decouples bending and twisting.

To further illustrate the effect of water on the system natural frequencies, we also plot the in-air root-loci in Figure 12 using $\rho_{\text{air}} = 1.225 \text{ kg/m}^3$. For this vessel speed sweep, the natural frequencies $\Im(p) = \Omega$ are much higher than the in-water results shown in Figure 10. The poles (p) stay nearly constant for this speed range because the variation of forces with respect to speed is small with the low air density. Damping, represented by $\eta_t = -2\xi/\Omega$, is lower in air than in water because the fluid damping terms, which are proportional to ρ_f , are smaller for air by about three orders of magnitude. The proportionality to ρ_f also means the speed-dependent effects in air for this dimensional speed range are less discernable than the in-water root loci in Figure 10. Frequencies in air are more separated compared to the submerged eigenvalues, so modal coalescence would not be captured by a purely in-air dynamic aeroelastic analysis. An in-air dynamic analysis would also fallaciously lead us to believe mode 1 (40.2 Hz) of the optimized hydrofoil will lock-in with the waterjet frequency (40.4 Hz). Because the solid-to-fluid density ratio (μ) is higher in air and our reduced velocity is fairly low by aircraft standards, this dynamic aeroelastic analysis in Figure 12 would be about the same as a typical modal analysis of the in-vacuum structural dynamics of the composite hydrofoil. The comparison between Figure 10 and 12 illustrates the importance of considering the in-water modal characteristics for design to capture natural frequencies, modal coalescence, and dynamic instabilities.

Based on the results from Figure 10, we recommend that the operator of the full-scale vessel with the optimized hydrofoil should avoid remaining at the full-scale 14 m/s speed to avoid this resonance based on interpolating root-loci and scaling the speed back up. This is similar to how some ship operators are advised to avoid idling the engine at a particular RPM.

Table 11 lists the dynamic constraint values to verify feasibility; violations are written in bold red font. The optimized design satisfies all constraints, while the baseline violates the frequency avoidance constraint (h_l) because of the waterjet and impeller frequencies. The base design also violates the total tip deflection constraints, so it is at risk of tip stall, as shown in Figure 7. This means there is potential for dynamic load amplifications and vibrations due to lock-in or resonance of a system mode of the baseline with these external sources because the wetted system natural frequency changed with flow speed to be in proximity (15%) with one of the critical frequencies. Our prediction of the lock-in of the baseline system modes with propulsion plant frequencies underscores the need for accurate simulations of the dynamic hydroelasticity of lightweight composites because traditional metallic marine structures are usually assumed to have constant natural frequency regardless of speed. Several researchers have

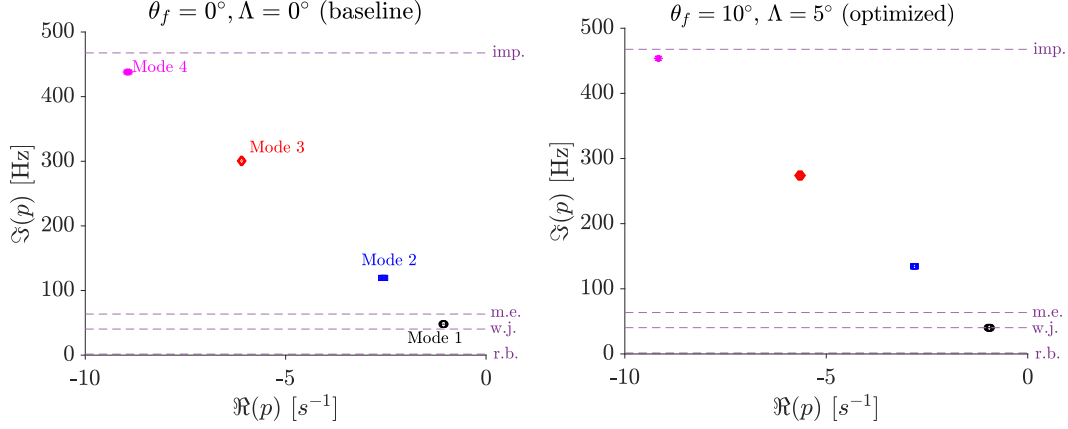


Figure 12: In-air root loci of the scaled baseline and optimized composite hydrofoil for the same speed sweep as shown in Figure 10 for in-water cases. Speed-dependent effects on p for this speed sweep are less apparent in air. Natural frequencies ($\Im(p)$) in air are much higher than the in-water values. The damping values ($\Re(p)$) are much lower in air than in water. An in-air analysis would erroneously predict that the optimized hydrofoil is at risk of lock-in with the waterjet (w.j.), but the hydrofoil operates in water, so it is not an issue. Natural frequencies in air are also more separated than in water; we would not assume any risk of modal coalescence for these flow speeds compared to in-water plots (Figure 10)

shown that speed impacts the system’s natural frequencies of marine structures, and this effect is more noticeable for low solid-to-fluid-added mass ratios [10, 11, 32, 56]. Neither design exhibits flutter (h_{flut}) since damping remains positive nor modal coalescence (h_g) since frequencies are not close enough with each other. Mean deformations and tip deformation constraints (h_{def} and h_{tip} respectively) are satisfied in both designs for the load scenario. For brevity, we do not list the $h_{\text{tip, stat}}$ constraint values since, by our definition, if h_{tip} is satisfied, then so is $h_{\text{tip, stat}}$.

Table 11: Dynamic constraint values show that the optimized design is feasible. If multiple values are listed, the ordered pair is bending and twisting. There is only an upper bound on these constraints, so negative values mean constraints are satisfied; red and bold means constraint violation

Constraint	Optimized			Baseline		Upper bound
	$C_L = 0.3$	$C_L = 0.6$	$C_L = 0.3$	$C_L = 0.6$		
h_{tip}	(-0.127, -5.815)	(-0.142, -1.507)	(0.025 , -2.190)	(-0.1153, 1.0468)		0
h_l	(-0.0003)	(-0.075)	(0.011 (mode 2 & waterjet))	(0.023 (mode 5 & impeller))		0
h_g	(-0.207)	(-0.114)	(-0.067)	(-0.084)		0
h_{def}	(-0.2989, -4.991)	(-0.29884, -4.9966)	(-0.299, -4.991)	(-0.297, -4.982)		0
h_{flut}	-17.877			-8.506		0

5 Discussion

5.1 Optimization algorithm

We used a heuristic optimization method appropriate for the reduced problem size that also allowed us design freedom to make adjustments to the “optimal” design based on physics not captured in the model, such as submergence and viscous effects. Because of these unmodeled physics, we did not employ a formal optimization algorithm such as a particle swarm method or genetic algorithm that may have resulted in highly swept designs with high θ_f . Instead, we used the merit functions and constraints to aid us in making more informed choices about the optimal design variables instead of a fully automated optimization.

Lastly, the computational time of this study was prohibitive for the current model since we used a scripted language (MATLAB). Cost is also increased for many discrete frequencies because each forcing frequency requires a solution of the governing equations. For our runs, we analyzed 2000 discrete frequencies between 0 and 200 Hz for the full-scale (0–346 Hz for the model scale). Each frequency response analysis for a design run costs 30 minutes in serial, as shown in Table 12. This study had at most 18 full runs if we used the naive approach, corresponding to 9 hours of simulations. These costs are not practical for design optimization, so we propose using a gradient-

Table 12: Computational metrics of the optimization for 18 potential design analyses (2 speeds and 9 designs). Runs are on 1 thread of Intel Core i7-8700 CPU @ 3.20GHz

Number of discrete frequencies per design analysis	Run time
2000	28 min 29 sec

based method to reduce the number of function evaluations in the future. We can also improve performance by using a compiled coding language and parallelizing processes.

5.2 Solution of design problem

Using our merit functions and constraints, we produced a composite hydrofoil with better steady and dynamic performance than the baseline design while satisfying steady lift requirements and avoiding excessive deflections, vibrations, noise, dynamic load amplification, dynamic instability, and accelerated fatigue. We had a reduced problem size with only three geometric and material design variables: angle of attack, fiber angle, and sweep angle.

Even though the essential marine lifting surface physics were considered in this study, a detailed optimization is necessary to capture more complex fluid and structural mechanics. In future studies, one would later refine the steady performance of this design using high-fidelity computational models to improve characteristics such as, but not limited to, lift-drag ratio, cavitation and flow separation avoidance, and material failure avoidance.

Most external excitation frequencies were considered, but viscous simulations would be needed to predict vortex shedding frequencies, which typically are coherent between

Strouhal numbers of 0.2–0.3. One could also make low-order approximations of these frequencies using relations between Reynolds numbers and vortex shedding.

More accurate damping forces from viscous and memory effects are also important to consider in higher fidelity since our model used inviscid theory but did not integrate the memory effects in time domain simulations [10]; both of these effects add to damping, so we are potentially overpredicting the amplitudes of motions by neglecting them.

Lifting surface wake-structure interaction with other components such as the hull or upstream structures may also need to be considered for the entire hull-foil system; we assumed uniform external flow, but viscous propulsor-rudder-hydrofoil-hull interactions may be significant as it has been shown that pressure fluctuations on a rudder from a propeller can result in unwanted vibrations and noise [57, 58]. We know that propellers with more skew (same as sweep) tend to have fewer vibration issues, so the spatially varying and non-uniform wake affects the optimal design variables of a composite hydrofoil when its performance as part of the whole vessel system is considered.

Depth and multiphase flow effects on added mass (and thus, system frequencies) and damping should also be considered in future optimizations because changing depth or small amounts of cavitation and ventilation may result in potential lock-in, resonance, or modal coalescence. Ideally, the hydrofoil is designed to avoid or delay cavitation and ventilation, but submergence depth will change with vessel motions and waves.

The coupling effect of vessel motion with the flexible hydrofoil should also be considered in the lifting surface design. We assumed a cantilevered hydrofoil, but hydrofoil motions will impact vessel motions and vice versa, resulting in different hydrofoil dynamics since the boundary conditions are different. Considering rigid body motion would allow us to consider body-freedom flutter in our lifting surface design. From this, one should consider the stability of the hydrofoil craft. Mader and Martins [59] formulated stability derivatives for aircraft, and a similar approach could be used for the hydrofoiling vessel.

We simplified the design study significantly by allowing no thickness, twist, or taper variables. Thickness has a crucial effect on the flexibility of a lifting surface since the bending and torsional stiffnesses are proportional to ϵ^4 . The effect of twist and taper on dynamic performance should also be investigated because they both alter the flow and structural performance.

Furthermore, the critical frequencies we designed for, such as cavitation, engine, and impeller frequencies, may not be constant throughout vessel operation though we assumed they were for simplicity. In the future, a probability density function could be used on frequency sources that are not fixed to model the change in excitation frequencies over the operating envelope. Despite this, the preliminary study served its purpose of design exploration and verification of our objectives and constraints. Practical applications of this model and method would be sweeping through design parameters and generating Pareto fronts to inform designers in what directions they should push their composite foil designs to achieve their desired steady and dynamic performances. Designers should use a higher-fidelity verification after this for the detail design phase.

6 Conclusions

This work represents the first steady and dynamic hydroelastic optimization of composite hydrofoils that uses both material and geometric design variables, considering modal coalescence and multiple operating points.

The optimized composite hydrofoil satisfies the design goal of meeting steady lift and deflection constraints while avoiding excessive vibration and dynamic load amplifications. Resonance frequencies are far enough from rigid body modes, engine frequencies, impeller shaft and impeller blade rate frequencies, cavity shedding frequencies, and wave frequencies. We also avoid frequency coalescence, which has not been addressed in previous hydrofoil design optimization.

The optimized hydrofoil is more damped at the critical frequencies and stiffer because of the slight backward sweep and slight forward fiber angle because of the relative contributions of generalized fluid forces in the coupled equations of motion as explained in Section 4. Severe fiber and sweep angles could result in frequency coalescence or lower critical instability speeds.

Marine composite lifting surface design differs from aircraft lifting surface design because it can exploit more significant hydrodynamic damping effects and avoid the greater fluid de-stiffening effects. This adds freedom to tune the dynamic hydroelastic performance in ways that cannot be realized in a less dense fluid such as air.

Considering multiple design speeds in optimization is critical for composite hydrofoils, mainly due to changing system natural frequencies, damping, and steady loads with respect to flow speed. We used a multipoint approach to consider the vessel operating profile. As shown in our baseline versus optimized results, the systems' dynamic characteristics changed with speed leading to resonance frequencies coming too close to the waterjet for the baseline.

Our optimized hydrofoil avoids resonance with the waterjet and all other considered external frequencies for our design speeds. However, in between design speeds, the resonance frequency of mode 2 crosses the waterjet, albeit with a positive damping loss factor. The transient resonance may be an issue, but it is still better than lock-in or resonance at a design point, so the optimized composite hydrofoil is still superior.

We especially need to consider how water lowers the system's natural frequencies and changes band gaps between modes in the optimization, which drastically changes the design problem from that of aircraft composites. When we compared in-water to in-air root-loci plots, we saw dramatic differences in the behavior of the system poles for both the baseline and optimized hydrofoils across the speed sweep.

Traditional approaches for analyzing the dynamic performance of structures perform only a modal or aeroelastic analysis, and aeroelastic analyses are less common. However, as we have shown, a dynamic hydroelastic evaluation is critical to predicting and avoiding excessive vibrations, accelerated fatigue, and dynamic load amplifications because water changes the modal behavior. As a result, neglecting the in-water dynamic performance and only performing a dry modal analysis can lead to erroneous results.

In summary, the newly developed objective function is an appropriate metric to capture vibrations of the composite hydrofoil. Combined with the newly developed

and previously devised constraints, we tailored a composite hydrofoil’s steady and dynamic performance to limit the static and dynamic deformations using a smaller set of design variables. This design optimization method can be generalized to many marine composite lifting surface problems, such as for the design of rudders, fin stabilizers, turbines, energy harvesting devices, energy saving devices, bilge keels, and hydrofoils that need to minimize (or maximize) static and dynamic deformations.

7 CRediT authorship contribution statement

Galen W. Ng: Methodology, Software, Validation, Formal analysis, Investigation, Visualization, Writing–Original Draft. **Joaquim R.R.A. Martins:** Methodology, Project administration, Supervision, Resources, Writing–Review and Editing. **Yin L. Young:** Methodology, Conceptualization, Project administration, Supervision, Funding acquisition, Resources, Writing–Review and Editing.

8 Declaration of Competing Interest

The authors declare that they have no known competing financial interests or personal relationships that could have appeared to influence the work reported in this paper.

9 Acknowledgments

Financial support for this research was provided by the U.S. Office of Naval Research (ONR) under Contracts N00014-16-1-2972 and N00014-18-1-2333 managed by Kelly Cooper. Galen W. Ng’s graduate education and research were supported in part by the OE&I Fellowship awarded by the Link Foundation and the Frank C. and Irving Pahlow Fellowship awarded by the Naval Architecture & Marine Engineering Department at The University of Michigan–Ann Arbor. This work was also supported in part through computational resources and services provided by Advanced Research Computing at the University of Michigan–Ann Arbor. The authors also would like to thank Eytan Adler for reviewing an earlier draft of this work.

10 Data Availability

Readers can contact the corresponding author for alternative means of obtaining the data presented here.

A Equations of Motion

A.1 Boundary Conditions for Cantilevered Hydrofoil

Geometric (wing clamped root, $y = 0$):

$$w = 0, \psi = 0, w' = 0, \psi' = 0 \quad (26)$$

Natural (wing free tip, $y = L$):

$$EI_s w''' + K_s \psi'' + abEI_s \psi''' = 0 \quad (27)$$

$$EI_s w'' + K_s \psi' + abEI_s \psi'' = 0 \quad (28)$$

$$GJ_s \psi' + K_s w'' - abEI_s w''' - S_s \psi''' = 0 \quad (29)$$

$$abK_s \psi' + abEI_s w'' + S_s \psi'' = 0 \quad (30)$$

References

- [1] Y. L. Young, M. R. Motley, R. Barber, E. J. Chae, N. Garg, Adaptive composite marine propulsors and turbines: Progress and challenges, *Applied Mechanics Reviews* 68 (2016) 060803. doi:doi:10.1115/1.4034659.
- [2] A. Mouritz, E. Gellert, P. Burchill, K. Challis, Review of advanced composite structures for naval ships and submarines, *Composite structures* 53 (2001) 21–42. doi:doi:10.1016/s0263-8223(00)00175-6.
- [3] N. Garg, B. W. Pearce, P. A. Brandner, A. W. Phillips, J. R. R. A. Martins, Y. L. Young, Experimental investigation of a hydrofoil designed via hydrostructural optimization, *Journal of Fluids and Structures* 84 (2019) 243–262. doi:doi:10.1016/j.jfluidstructs.2018.10.010.
- [4] E. Livne, T. A. Weisshaar, Aeroelasticity of nonconventional airplane configurations — past and future, *Journal of Aircraft* 40 (2003) 1047–1062.
- [5] T. Yamatogi, H. Murayama, K. Uzawa, K. Kageyama, N. Watanabe, Study on cavitation erosion of composite materials for marine propeller, in: *The 17th International Conference on Composites (ICCM-17)*, Edinburgh, UK, 2009.
- [6] Y. L. Young, C. M. Harwood, M. F. Montero, J. C. Ward, S. L. Ceccio, Ventilation of lifting bodies: Review of the physics and discussion of scaling effects, *Applied Mechanics Reviews* 69 (2017) 010801.
- [7] P. de Jong, C. Kent, B. Bouscasse, F. Gerhardt, O. A. Hermundstad, T. Katayama, M. Minoura, B.-W. Nam, Y. L. J. Young, *The Seakeeping Committee Final Report and Recommendations to the 29th ITTC*, Technical Report, 2021.
- [8] Y. L. Young, Hydroelastic response of lifting bodies in separated flows, in: *NATO-AVT-307: Symposium on Separated Flow: Prediction, Measurement and Assessment for Air and Sea*, Trondheim, Norway, 2019.
- [9] C. M. Harwood, M. Felli, M. Falchi, N. Garg, S. L. Ceccio, Y. L. Young, The hydroelastic response of a surface-piercing hydrofoil in multiphase flows. part 2. modal parameters and generalized fluid forces, *Journal of Fluid Mechanics* 884 (2019). doi:doi:10.1017/jfm.2019.871.

- [10] G. W. Ng, A. S. Vishneek, J. R. R. A. Martins, Y. L. Young, Scaling the dynamic response and stability of composite hydrodynamic lifting surfaces, *Composite Structures* (2022) 115148. doi:doi:10.1016/j.compstruct.2021.115148.
- [11] E. J. Chae, Y. L. Young, Influence of spanwise flexibility on steady and dynamic responses of airfoils vs hydrofoils, *Physics of Fluids* 33 (2021) 067124.
- [12] A. Phillips, R. Cairns, C. Davis, P. Norman, P. Brandner, B. Pearce, Y. L. Young, Effect of material design parameters on the forced vibration response of composite hydrofoils in air and in water, in: *Fifth International Symposium on Marine Propulsors*, Espoo, Finland, 2017.
- [13] M. R. Kramer, Z. Liu, Y. L. Young, Free vibration of cantilevered composite plates in air and in water, *Composite Structures* 95 (2013) 254–263. doi:doi:10.1016/j.compstruct.2012.07.017.
- [14] D. B. Dittenber, *Fatigue of polymer composites: Life prediction and environmental effects*, West Virginia University, 2010.
- [15] Y. Young, T. Wright, H. Yoon, C. Harwood, Dynamic hydroelastic response of a surface-piercing strut in waves and ventilated flows, *Journal of Fluids and Structures* 94 (2020) 102899. URL: <https://linkinghub.elsevier.com/retrieve/pii/S0889974619305559>. doi:doi:10.1016/j.jfluidstructs.2020.102899.
- [16] D. T. Akcabay, E. J. Chae, Y. L. Young, A. Ducoin, J. A. Astolfi, Cavity induced vibration of flexible hydrofoils, *Journal of Fluids and Structures* 49 (2014) 463–484. doi:doi:10.1016/j.jfluidstructs.2014.05.007.
- [17] A. Champneys, *Dynamics of Parametric Excitation*, Springer New York, New York, NY, 2011, pp. 183–204. doi:doi:10.1007/978-1-4614-1806-1_13.
- [18] T. E. Rajaomazava, M. Benaouicha, J.-A. Astolfi, A.-O. Boudraa, Frequency and amplitude modulations of a moving structure in unsteady non-homogeneous density fluid flow, *Fluids* 6 (2021) 130.
- [19] P. K. Besch, Y.-N. Liu, Hydroelastic design of subcavitating and cavitating hydrofoil strut systems, Technical Report, Naval Ship Research and Development Center, Bethesda, Maryland, U.S.A., 1974.
- [20] D. T. Akcabay, Y. L. Young, Steady and dynamic hydroelastic behavior of composite lifting surfaces, *Composite Structures* 227 (2019) 111240. doi:doi:10.1016/j.compstruct.2019.111240.
- [21] Y. Liao, J. R. R. A. Martins, Y. L. Young, 3-D high-fidelity hydrostructural optimization of cavitation-free composite lifting surfaces, *Composite Structures* 268 (2021) 113937. doi:doi:10.1016/j.compstruct.2021.113937.

- [22] S. Volpi, M. Diez, F. Stern, Multidisciplinary Design Optimization of a 3D Composite Hydrofoil via Variable Accuracy Architecture, American Institute of Aeronautics and Astronautics, 2018. doi:doi:doi:10.2514/6.2018-4173.
- [23] M. T. Herath, B. G. Prusty, A. W. Phillips, N. St. John, Structural strength and laminate optimization of self-twisting composite hydrofoils using a genetic algorithm, Composite Structures 176 (2017) 359 – 378. doi:doi:10.1016/j.compstruct.2017.05.012.
- [24] N. Garg, G. K. W. Kenway, J. R. R. A. Martins, Y. L. Young, High-fidelity coupled hydrostructural optimization of a 3-D hydrofoil, in: Proceedings of the International Symposium on Transport Phenomena and Dynamics of Rotating Machinery, 2016.
- [25] N. Garg, G. K. W. Kenway, J. R. R. A. Martins, Y. L. Young, High-fidelity multipoint hydrostructural optimization of a 3-D hydrofoil, Journal of Fluids and Structures 71 (2017) 15–39. doi:doi:10.1016/j.jfluidstructs.2017.02.001.
- [26] B. Niu, X. He, Y. Shan, R. Yang, On objective functions of minimizing the vibration response of continuum structures subjected to external harmonic excitation, Structural and Multidisciplinary Optimization 57 (2018) 2291–2307. URL: <https://doi.org/10.1007/s00158-017-1859-1>. doi:doi:10.1007/s00158-017-1859-1.
- [27] X. D. He, Y. Hong, R. G. Wang, Hydroelastic optimisation of a composite marine propeller in a non-uniform wake, Ocean Engineering 39 (2012) 14–23. doi:doi:<https://doi.org/10.1016/j.oceaneng.2011.10.007>.
- [28] M. L. Mulcahy, P. Croaker, D. G. McGuckin, P. A. Brandner, N. Kississoglou, Optimisation applied to composite marine propeller noise, in: INTER-NOISE and NOISE-CON Congress and Conference Proceedings, volume 249, Institute of Noise Control Engineering, 2014, pp. 4012–4019.
- [29] E. E. Bachynski, Y. L. Young, R. W. Yeung, Analysis and optimization of a tethered wave energy converter in irregular waves, Renewable Energy 48 (2012) 133–145. doi:doi:10.1016/j.renene.2012.04.044.
- [30] E. Jonsson, G. K. W. Kenway, G. J. Kennedy, J. R. R. A. Martins, Development of flutter constraints for high-fidelity aerostructural optimization, in: 18th AIAA/ISSMO Multidisciplinary Analysis and Optimization Conference, Denver, CO, 2017. AIAA 2017-4455.
- [31] D. T. Akcabay, Y. L. Young, Influence of material anisotropy on the hydroelastic response of composite plates in water, in: Proc.SPIE, volume 10596, Denver, CO, 2018, pp. 10596–10596–15. doi:doi:10.1117/12.2304361.
- [32] D. T. Akcabay, Y. L. Young, Material anisotropy and sweep effects on the hydroelastic response of lifting surfaces, Composite Structures 242 (2020) 112140. doi:doi:10.1016/j.compstruct.2020.112140.

- [33] Y. L. Young, J. Chang, S. M. Smith, J. A. Venning, B. W. Pearce, P. A. Brandner, The influence of fluid-structure interaction on cloud cavitation about a stiff hydrofoil. part 3, *Journal of Fluid Mechanics* (2021).
- [34] O. M. Faltinsen, *Hydrodynamics of high-speed marine vehicles*, Cambridge University Press, 2006. doi:doi:10.1017/CBO9780511546068.
- [35] Y. L. Young, Z. Liu, M. Motley, Influence of material anisotropy on the hydroelastic behaviors of composite marine propellers, in: *27th Symposium on Naval Hydrodynamics*, 2008.
- [36] I. Lottati, Flutter and divergence aeroelastic characteristics for composite forward swept cantilevered wing, *Journal of Aircraft* 22 (1985) 1001–1007. doi:doi:10.2514/3.45238.
- [37] T. Theodorsen, *General Theory of Aerodynamic Instability and the Mechanism of Flutter*, Technical Report Rept. 496, NACA, 1934.
- [38] E. C. Yates, Modified-strip-analysis method for predicting wing flutter at subsonic to hypersonic speeds, *Journal of Aircraft* 3 (1966) 25–29. doi:doi:10.2514/3.43702.
- [39] R. L. Bisplinghoff, H. Ashley, *Principles of Aeroelasticity*, Dover Publications, Inc., 1975.
- [40] E. Dowell, E. Crawley, H. Curtiss, D. Peters, R. Scanlan, F. Sisto, *A Modern Course in Aeroelasticity*, Springer Netherlands, 1995.
- [41] Y. Liao, N. Garg, J. R. R. A. Martins, Y. L. Young, Viscous fluid structure interaction response of composite hydrofoils, *Composite Structures* 212 (2019) 571–585. doi:doi:10.1016/j.compstruct.2019.01.043.
- [42] G. Beaulieu, D. Noiseux, Computation of the modes and polar moment of inertial of the blades of an hawt, NASA. Lewis Research Center Wind Turbine Dyn. (1981).
- [43] J. R. R. A. Martins, A. Ning, *Engineering Design Optimization*, Cambridge University Press, 2021. URL: <https://mdobook.github.io>. doi:doi:10.1017/9781108980647.
- [44] A. B. Lambe, J. R. R. A. Martins, G. J. Kennedy, An evaluation of constraint aggregation strategies for wing box mass minimization, *Structural and Multidisciplinary Optimization* 55 (2017) 257–277. doi:doi:10.1007/s00158-016-1495-1.
- [45] D. T. Akcabay, Y. L. Young, Parametric excitations and lock-in of flexible hydrofoils in two-phase flows, *Journal of Fluids and Structures* 57 (2015) 344–356.
- [46] R. Zubaly, *Applied Naval Architecture*, Cornell Maritime Press, 1996. URL: <https://books.google.com/books?id=GMoAAAAACAAJ>.

- [47] R. P. Liem, J. R. R. A. Martins, G. K. Kenway, Expected drag minimization for aerodynamic design optimization based on aircraft operational data, *Aerospace Science and Technology* 63 (2017) 344–362. doi:doi:10.1016/j.ast.2017.01.006.
- [48] M. F. Ashby, D. CEBON, Materials selection in mechanical design, *Le Journal de Physique IV* 3 (1993) C7–1.
- [49] S. Kellas, J. Morton, Strength scaling in fiber composites, *AIAA Journal* 30 (1992) 1074–1080. doi:doi:10.2514/3.11029.
- [50] J. Morton, Scaling of impact-loaded carbon-fiber composites, *AIAA Journal* 26 (1988) 989–994. doi:doi:10.2514/3.10001.
- [51] S. M. Smith, J. A. Venning, B. W. Pearce, Y. L. Young, P. A. Brandner, The influence of fluid–structure interaction on cloud cavitation about a stiff hydrofoil. part 1., *Journal of Fluid Mechanics* 896 (2020) A1. doi:doi:10.1017/jfm.2020.321.
- [52] S. M. Smith, J. A. Venning, B. W. Pearce, Y. L. Young, P. A. Brandner, The influence of fluid–structure interaction on cloud cavitation about a flexible hydrofoil. part 2., *Journal of Fluid Mechanics* 897 (2020) A28. doi:doi:10.1017/jfm.2020.323.
- [53] Z. Lyu, Z. Xu, J. R. R. A. Martins, Benchmarking optimization algorithms for wing aerodynamic design optimization, in: *Proceedings of the 8th International Conference on Computational Fluid Dynamics*, Chengdu, Sichuan, China, 2014. ICCFD8-2014-0203.
- [54] D. McLean, *Understanding Aerodynamics: arguing from the real physics*, Wiley, West Sussex, UK, 2013.
- [55] Y. Liao, J. R. R. A. Martins, Y. L. Young, Sweep and anisotropy effects on the viscous hydroelastic response of composite hydrofoils, *Composite Structures* 230 (2019) 111471. doi:doi:10.1016/j.compstruct.2019.111471.
- [56] E. J. Chae, D. T. Akcabay, Y. L. Young, Influence of flow-induced bend–twist coupling on the natural vibration responses of flexible hydrofoils, *Journal of Fluids and Structures* 69 (2017) 323–340. doi:doi:10.1016/j.jfluidstructs.2016.12.008.
- [57] W. Zhang, X. Ning, F. Li, H. Guo, S. Sun, Vibrations of simplified rudder induced by propeller wake, *Physics of Fluids* 33 (2021) 083618.
- [58] R. Muscari, G. Dubbioso, A. Di Mascio, Analysis of the flow field around a rudder in the wake of a simplified marine propeller, *Journal of Fluid Mechanics* 814 (2017) 547–569. doi:doi:10.1017/jfm.2017.43.
- [59] C. A. Mader, J. R. R. A. Martins, Computing stability derivatives and their gradients for aerodynamic shape optimization, *AIAA Journal* 52 (2014) 2533–2546. doi:doi:10.2514/1.J052922.